1   **Title:** Acute Viral Infection Accelerates Neurodegeneration in a Mouse Model of ALS

2

3   **One Sentence Summary:** Acute viral infection with influenza A virus and SARS-CoV-2

4   accelerates the progression of ALS in SOD1[G93A] mice.

5

6   **Authors:** Art Marzok[1†], Jonathan P. Mapletoft[1†], Braeden Cowbrough[1], Daniel B. Celeste[1],

7   Michael R. D'Agostino[1], Jann C. Ang[1], Andrew T. Chen[1], Vithushan Surendran[1], Anna Dvorkin-

8   Gheva[2], Ali Zhang[1], Hannah D. Stacey[1], Mannie Lam[1], Yasmine Kollar[1], Kevin R. Milnes[1], Sam

9   Afkhami[1], Matthew S. Miller[1,3,*]

10

11   †Denotes first author

12   * Denotes corresponding author. mmiller@mcmaster.ca

13

14   **Affiliations:**

15   1) M. G. DeGroote Institute for Infectious Disease Research, Department of Biochemistry &

16   Biomedical Sciences, McMaster University, Hamilton, Ontario, L8S 4K1, Canada

17

18   2) Firestone Institute for Respiratory Health, Division of Respirology, Department of Medicine,

19   McMaster University, Hamilton, Ontario, L8M 4A6, Canada

20

21   3) Lead contact

22

23

24 **Summary:**

25

26 While several viral infections have been associated with amyotrophic lateral sclerosis (ALS), the

27 mechanism(s) through which they promote disease has remained almost entirely elusive. This

28 study investigated the impact of common, acute viral infections prior to disease onset on ALS

29 progression in the SOD1^{G93A} mouse model. A single sublethal infection prior to onset of ALS

30 clinical signs was associated with markedly accelerated ALS disease progression characterized

31 by rapid loss of hindlimb function. Prior infection resulted in gliosis in the lumbar spine and

32 upregulation of transcriptional pathways involved in inflammatory responses, metabolic

33 dysregulation, and muscular dysfunction. Therapeutic suppression of gliosis with an anti-

34 inflammatory small molecule, or administration of a direct-acting antiviral, was associated with

35 significantly improved ALS clinical signs, akin to what was observed in uninfected animals. This

36 study provides causal and mechanistic evidence that the immune response elicited by acute viral

37 infections may be an important etiological factor that alters ALS disease trajectory, and provides

38 insight into novel therapeutic and preventative strategies for ALS.

39

40 **Keywords:** Amyotrophic lateral sclerosis, ALS, neurodegeneration, SOD1^{G93A}, viral infection,

41 influenza, influenza A virus, SARS-CoV-2, neuroinflammation, gliosis.

42

43 **Introduction**

44

45 Amyotrophic Lateral Sclerosis (ALS) is an incurable motor neuron disease which is

46 characterized by progressive deterioration of upper and lower motor neurons leading to muscle

47   wasting and paralysis[1,2]. The disease is remarkably heterogeneous in age-of-onset and in

48   presentation of symptoms, even for individuals harboring the same ALS-associated mutations[3–6].

49   A combination of genetic and environmental factors are therefore believed to play critical roles

50   in disease development and progression[6].

51

52   Viruses have been characterized as environmental risk factors for ALS and other

53   neurodegenerative diseases[7]. However, several of these associations have been erroneous and

54   study designs have led to an enrichment bias favoring viruses that cause chronic/latent and

55   neurotropic infections[8]. Poliovirus was the first virus associated with ALS due to its

56   neurotropism and ability to cause post-poliomyelitis which phenotypically resembles ALS[7].

57   Subsequent studies have demonstrated that the enterovirus-associated 3C protease is able to

58   cleave TAR DNA binding protein 43 (TDP-43), a pathophysiological feature observed in 97% of

59   ALS cases[9,10]. Additionally, a sublethal intracerebroventricular infection with the coxsackie virus

60   B3, a type of enterovirus, accelerated ALS disease progression in SOD1^{G85R} mice[11]. There has

61   also been compelling evidence linking endogenous retroviruses such as Human Endogenous

62   Retrovirus-K (HERV-K) to ALS, as transgenic mice constitutively expressing the *env* protein of

63   HERV-K develop symptoms of progressive motor neuron disease[12,13]. Such observations have

64   supported on-going clinical trials evaluating antiretroviral therapy in ALS patients[14–16].

65

66   Although common, acute non-neurotropic viral infections may also be associated with ALS and

67   other neurodegenerative diseases, they have been widely understudied since ubiquitous

68   infections, especially those that occur significantly prior to the onset of disease (i.e. "hit-and-

69   run"), are difficult to associate using conventional epidemiological approaches. This, is due, in

70　part, to the fact that these viruses are likely cleared long before ALS symptom onset begins and

71　seropositivity is high amongst the general population. Elegant recent work using data from

72　biobank repositories across multiple countries showed an increased risk of developing

73　neurodegenerative diseases such as ALS from acute viral infections, with increased hazard ratios

74　persisting even 15 years following infection[17]. However, much remains to be understood

75　regarding the mechanism through which viral infections impact ALS.

76

77　Influenza A viruses (IAV) are a group of single-stranded RNA viruses which predominantly

78　result in acute, self-limiting respiratory infections[18]. Infection is associated with systemic

79　elevation of pro-inflammatory soluble mediators which can potentiate neuroinflammation.

80　Indeed, non-neurotropic IAV strains have been shown to directly induce long-lasting

81　neuroinflammation with accompanying decreases in dendritic spine density to hippocampal

82　neurons – a typical hallmark of neurodegeneration[19]. The COVID-19 pandemic, caused by

83　SARS-CoV-2, has also led to lasting neurological manifestations during "long COVID", with

84　studies showing long-term neurological sequelae in approximately 33% of recovered COVID-19

85　patients, even 6 months post-infection[20,21]. In addition, SARS-CoV-2 RNA and antigens have

86　been found in the CNS of COVID-19 patients[22]. Strikingly, SARS-CoV-2 infection has already

87　been associated with increased susceptibility to Parkinsons disease as well as other

88　neurodegenerative diseases[23,24]. In addition to inducing pathological immune responses, viral

89　infections have been shown to perturb many of the same pathophysiological pathways

90　underlying motor neuron death in ALS[8].

91

92   A common mechanism through which diverse viral infections may exacerbate ALS is through

93   the induction of aberrant host immune responses that can lead to neuroinflammation[25].

94   Inflammation is a hallmark characteristic of both viral infections and ALS, with elevated

95   peripheral inflammation and neuroinflammation positively correlating with disease severity[26].

96   ALS patients often experience heightened levels of gliosis and pro-inflammatory cytokines in the

97   peripheral blood and cerebral spinal fluid (CSF)[27]. Given this close interplay between

98   inflammation and ALS, common acute viral infections may exacerbate ALS disease progression

99   through further stimulating the immune system and elevating pre-existing CNS and systemic

100   inflammatory mediators. However, many studies suggesting an association between ALS and

101   prior infection have been correlative and lack mechanistic insights as to how viral infections

102   potentiate disease. Furthermore, it remains unclear whether common acute respiratory infections

103   impact ALS disease progression, and the mechanism(s) through which this might occur.

104

105   Here, we demonstrate that a single acute infection with either IAV or SARS-CoV-2 during the

106   pre-clinical stages of ALS disease significantly accelerates ALS progression in SOD1^{G93A} mice.

107   Interestingly, intramuscular administration of inactivated IAV resulted in similar disease

108   acceleration, a phenomenon not observed following intranasal delivery. Mechanistically, this

109   acceleration of ALS progression was accompanied by activation of microglia and astrocytes in

110   the lumbar spinal cord of SOD1^{G93A} mice following infection, and transcriptomic enrichment of

111   pathways relating to inflammation, immunity, and muscular dysfunction. Importantly, our

112   findings further reveal that the inhibition of microglial activation during infection, or treatment

113   with antivirals, helps mitigate ALS acceleration in these mice. This study thus provides direct

114 causal and mechanistic evidence of acute respiratory infections exacerbating ALS progression in

115 a mouse model of disease.

116

117 **Results**

118

119 **Acute IAV infection prior to ALS onset accelerates disease progression in SOD1^{G93A} mice.**

120

121 Despite over 30 years of reported associations between viral infections and ALS, no prior studies

122 have systematically explored the role of acute, non-neurotropic viral infections on the

123 progression of ALS. To address this critical gap, we used influenza A virus (IAV) as a model

124 given its ubiquity. Indeed, most individuals have experienced their first influenza infection by

125 five years of age, and are re-infected regularly throughout the course of their life[28–30]. To

126 determine whether IAV infection during the pre-clinical stages of ALS disease accelerates the

127 onset and/or progression of ALS, wildtype BL6SJL (WT) and B6SJL-TgN(SOD1*G93A)1Gur

128 (SOD1^{G93A}) mice were infected intranasally (i.n.) with a sublethal dose (300 PFU) of mouse-

129 adapted influenza A virus (strain A/Puerto Rico/8/1934 H1N1, (PR8)) at day 60 of age (**Fig.**

130 **1A**). This age was chosen based on the well-characterized kinetics of disease onset in this model

131 as reported in the literature (typically, early onset is detectable at day 90)[31]. Indeed, there were

132 no statistical differences observed between WT and SOD1^{G93A} mice in rotarod performance at

133 day 60 of age (mean 51.1 and 47.9 seconds), indicating no observable phenotypic signs of ALS

134 onset in SOD1^{G93A} mice (**Fig. 1B**). Following infection, no infectious virus was detected in lung

135 and brain homogenates of WT or SOD1^{G93A} mice at 14 days post-infection (dpi) (**Supplemental**

136 **Fig. 1A and 1B**). This is consistent with previous literature demonstrating that infection with this

137   strain of IAV is acute and non-neurotropic[32]. After recovering from infection, mice were tested

138   on the rotarod apparatus to measure motor function and general coordination and were compared

139   to uninfected controls. Mice were tested weekly and the latency for falling off the rotating rod

140   was recorded. Previously infected SOD1^{G93A} mice performed significantly worse on the rotarod

141   test, as measured by the weeks elapsed to reach 50% of their initial fall time, when compared to

142   uninfected SOD1^{G93A} mice (Mean 9.137 weeks and 11.182 weeks, p = 0.0002) (**Fig. 1C**). In

143   addition, these mice reached endpoint due to ALS clinical signs, as defined by complete hind-

144   limb paralysis and loss of the righting reflex, significantly faster than uninfected SOD1^{G93A} mice

145   (**Fig. 1D**). Taken together, these data demonstrate that a single, acute, sublethal IAV infection

146   during the pre-clinical stages of ALS significantly accelerates disease progression.

147

148   **WT and SOD1^{G93A} mice experience similar acute disease characteristics following viral**

149   **infection.**

150

151   Given that a single acute IAV infection was associated with marked acceleration in ALS disease

152   progression, we next sought to determine whether this was related to differences in infection

153   kinetics and/or severity in SOD1^{G93A} mice compared to WT controls. To this end, mice were

154   infected i.n. with a sublethal dose of IAV at day 60 of age and were subsequently monitored for

155   influenza-associated morbidity and mortality. Both IAV-infected WT and SOD1^{G93A} mice had

156   similar weight loss kinetics, with peak weight loss at 8 dpi (**Fig. 1E**). Likewise, no significant

157   differences in survival following acute infection were observed (**Fig. 1F**).

158

159   Consistent with the lack of observed differences in infection kinetics and severity, there were no

160   differences in lung viral titres between SOD1^{G93A} and WT mice as assessed by plaque forming

161   unit (PFU) assay during peak viral load (4 dpi) (**Fig. 1G**). These findings were further confirmed

162   using mouse embryonic fibroblasts (MEFs) derived from SOD1^{G93A} and WT mice, as infection

163   with IAV at a multiplicity of infection (MOI) of 3 resulted in no significant differences in IAV

164   titres in the supernatant of infected cells over the course of 48 hours (**Fig. 1H**). Taken together,

165   these results suggest that both WT and SOD1^{G93A} mice resolve acute infection similarly,

166   indicating that SOD1^{G93A} mice are not inherently more susceptible to IAV infection and thus,

167   that differences in acute infection characteristics are unlikely to explain the observed acceleration

168   in ALS disease progression.

169

170   **WT and SOD1^{G93A} mice mount similar antiviral- and pro-inflammatory responses following**

171   **IAV infection.**

172

173   Peripheral- and neuro-inflammation are key hallmarks of ALS and related neurodegenerative

174   disorders, correlating with disease severity in both patients and pre-clinical models, including

175   SOD1^{G93A} mice[26,27]. Additionally, there is growing recognition that the cGAS-STING pathway,

176   which is involved in the host antiviral response, is important for disease progression[33–35]. Given

177   that acute viral infections induce pro-inflammatory and antiviral responses, we next sought to

178   determine whether differences exist in such responses following IAV infection in WT and

179   SOD1^{G93A} mice. To this end, WT and SOD1^{G93A} MEFs were stimulated with an MOI of 10 of

180   UV-inactivated IAV (**Fig. 2A**). Viral inactivation was performed to eliminate antiviral gene

181   antagonism by virally-encoded proteins which would confound measurement of the host antiviral

182   response[36]. RNA was isolated from cellular lysates collected at 4-, 8-, and 24-hours post-

183   infection for RT-qPCR to determine relative gene expression values for bona fide antiviral genes,

184   including interferon-induced transmembrane protein 3 (*IFITM3*), RIG-I (*DDX58*), and

185   interferon-induced protein with tetratricopeptide repeats 1 (*IFIT1*). Relative expression levels

186   were determined using the $2^{-\Delta\Delta Ct}$ method and values were normalized to untreated, uninfected

187   WT MEFs (**Fig. 2B)**. As expected, all antiviral genes were upregulated following exposure to

188   inactivated virus in a time-dependent manner, but there were no significant differences in

189   antiviral expression levels between the two infected groups (**Fig. 2B**).

190

191   To assess pro-inflammatory cytokines/chemokines induced by IAV infection, a 32-plex pro-

192   inflammatory cytokine/chemokine array was performed on the supernatants collected following

193   UV-inactivated IAV stimulation of WT and SOD1^{G93A} MEFs (**Fig. 2A**). Compared to baseline

194   untreated MEFs, both WT and SOD1^{G93A} MEFs produced elevated levels of inflammatory

195   analytes at all timepoints, with expression levels increasing throughout the duration of the

196   stimulation (**Fig. 2C**). Once again, we observed no significant differences in the magnitude of

197   cytokine/chemokine examined at each timepoint for IAV-stimulated WT and SOD1^{G93A} MEFs.

198   To determine whether these similarities persisted *in vivo*, WT and SOD1^{G93A} mice were infected

199   i.n. with a sublethal dose of IAV at day 60 of age and lung and brain homogenates were collected

200   at 4- and 30- dpi (**Fig. 2D**). As expected, multiple pro-inflammatory analytes were similarly

201   elevated in the lungs (**Fig. 2E, left panel**) and brain (**Fig. 2F, left panel**) of WT and SOD1^{G93A}

202   mice following IAV infection at 4 dpi, as compared to uninfected mice. Strikingly, several of

203   these analytes remained elevated at 30 dpi in the lung (**Fig. 2E, right panel**) and brain (**Fig. 2F,**

204   **right panel**), well after resolution of IAV infection (**Supplemental Fig. 1**). In concordance with

205 the observations in MEFs, there were no significant differences in pro-inflammatory

206 cytokine/chemokine relative expression levels between IAV-infected WT and SOD1^{G93A} mice.

207 Taken together, these data suggest that WT and SOD1^{G93A} mice mount similar antiviral and

208 inflammatory responses to IAV infection – results that are in alignment with the observed

209 similarities weight loss and viral replication between the two genotypes.

210

211 **Virus-induced systemic and neuroinflammation is associated with accelerated ALS disease**

212 **progression**

213

214 Having established that IAV infection accelerates ALS disease progression in SOD1^{G93A} mice,

215 we next went on to determine the contribution of the immune response stimulated by the virus on

216 disease acceleration. By inactivating the virus prior to inoculation, the contribution of viral

217 replication to observed phenotypes is eliminated, and any differences can be attributed primarily

218 to the host response resulting from viral detection. To this end, we administered 50 µg of

219 formalin-inactivated IAV intramuscularly (i.m.) within the quadricep muscle and compared these

220 to mice receiving i.m. vehicle control (equimolar formalin diluted in PBS) (**Fig. 3A**). We

221 observed no weight loss following inoculation during the 2-week monitoring period (data not

222 shown). Mice were then subjected to the rotarod test and monitored until endpoint was reached

223 due to progression of ALS clinical signs. SOD1^{G93A} mice administered formalin-inactivated IAV

224 i.m. performed significantly worse on the rotarod test, reaching 50% of their initial fall time

225 significantly faster than mice administered i.m. vehicle control (**Fig. 3B**). Additionally, this route

226 of administration significantly shortened lifespan of SOD1^{G93A} mice compared to those

227 administered vehicle control (**Fig. 3C**). Since IAV infection results in considerable systemic

228 inflammation, and the hindlimbs where inactivated IAV was injected is the site where ALS

229 disease manifests in the SOD1^{G93A} mouse model, we set out to determine whether local

230 inflammation in tissues other than the quadriceps also accelerated disease. To this end, we

231 administered inactivated IAV or vehicle control intranasally (**Fig. 3A**). Similar to inactivated

232 IAV administered i.m., no weight loss was observed (data not shown). However, in contrast to

233 inactivated IAV given i.m., when an equal dose of formalin-inactivated IAV was administered

234 i.n., there were no significant differences in rotarod performance (**Fig. 3D**) and there were no

235 differences in survival due to ALS clinical signs for mice administered inactivated IAV i.n.

236 compared to mice administered vehicle control (**Fig. 3E**).

237

238 To measure the magnitude of systemic and neuroinflammation induced by administering

239 inactivated IAV relative to a bona fide IAV infection, we administered 50 µg inactivated IAV

240 either i.n. or i.m. and compared these mice to those given 300 PFU i.n. of live IAV. At 4 days

241 post-administration, serum and brain homogenates were obtained and a 32-plex

242 cytokine/chemokine analysis was conducted (**Fig. 3F**). In serum, we observed the highest

243 magnitude of pro-inflammatory analytes in mice infected with 300 PFU IAV. Additionally, an

244 intermediate phenotype was observed in SOD1^{G93A} mice receiving inactivated IAV i.m., as

245 levels were higher than mice administered inactivated IAV i.n. (**Fig. 3G**). The more pronounced

246 inflammatory responses induced by live virus infection and i.m. administration of inactivated

247 virus were therefore associated with disease progression relative to i.n. administration of

248 inactivated IAV, which induced minimal systemic and neuroinflammation and did not accelerate

249 disease.

250

251 Collectively, these data suggest infection-induced immunity appears to be an important factor in

252 eliciting ALS disease acceleration. This is especially evident when inflammation is systemic or

253 localized within disease susceptible tissues, such as the hind-limbs of SOD1^{G93A} mice.

254

255 **Acute IAV infection is associated with elevated gliosis and ALS-related transcripts in the**

256 **lumbar spine.**

257

258 Neuroinflammation and pathological non-cell autonomous processes such as aberrant glial cell

259 activation are critical drivers of motor neuron degeneration in patients and pre-clinical models[37].

260 In the SOD1^{G93A} model, selective ablation of this mutant gene in microglia and astrocytes leads

261 to slower disease progression, suggesting a key role for these cells in ALS pathophysiology[38,39].

262 Furthermore, it has been well established that neuroinflammation can prime microglia to a

263 predominantly pathogenic cytotoxic/pro-inflammatory M1 phenotype[40]. Given these findings,

264 and that acute infection with a non-neurotropic strain of IAV was associated with sustained

265 increased levels of pro-inflammatory cytokines/chemokines in the brain (**Fig. 2F**), we next

266 investigated whether IAV infection induced inflammation and/or gliosis in the lumbar spine of

267 SOD1^{G93A} mice.

268

269 To characterize the inflammatory profile, a 32-plex pro-inflammatory cytokine/chemokine

270 analysis was performed on lumbar spine homogenates at 4 dpi (during acute infection) and day

271 120 of age (60 dpi – late-stage ALS disease). A trend towards increased secretion of eotaxin, IL-

272 6, IL-10, and interferon gamma produced protein-10 (IP-10) was observed in IAV infected

273 SOD1^{G93A} mice compared to uninfected mice at 4 dpi (**Supplemental Fig. 2A**). Next, we went

274   on to assess whether inflammatory cytokine/chemokine expression levels following IAV

275   infection were sustained even after the resolution of acute infection. We observed low levels of

276   pro-inflammatory cytokines in the lumbar spine of WT mice for all analytes assessed at day 120

277   of age (60 dpi), regardless of previous IAV infection. SOD1^{G93A} mice had higher expression

278   levels of multiple analytes, however, we observed no significant differences between previously

279   IAV-infected and uninfected SOD1^{G93A} mice at this timepoint (**Supplemental Fig. 2B**),

280   suggesting that inflammatory cytokine/chemokine levels normalize to uninfected levels by 60

281   dpi.

282

283   To assess the level of gliosis in the lumbar spine, WT and SOD1^{G93A} mice were infected i.n. with

284   a sublethal dose of IAV at day 60 of age and immunohistochemistry was performed at day 90 of

285   age (30 dpi) (**Fig. 4A**). This timepoint was chosen as sustained peripheral and central

286   inflammation following sublethal IAV infection was observed (**Fig 2E and 2F**), and that day 90

287   typically corresponds to onset of ALS clinical signs in this model. Spinal sections were isolated

288   and fixed sections were probed with anti-GFAP and anti-Iba1 antibodies to measure levels of

289   astrocyte and microglia activation, respectively. In agreement with previously published studies,

290   elevated levels of gliosis as measured by the number of GFAP+ astrocytes (**Fig. 4B**) and Iba1+

291   microglia (**Fig. 4C**) were observed in lumbar spines from uninfected SOD1^{G93A} mice in

292   comparison to uninfected WT controls. Strikingly, whereas there we no significant increases in

293   gliosis in WT mice following IAV infection, this single infection event 30 days earlier was

294   associated with both a marked increase in GFAP+ astrocytes, and a significant increase in Iba1+

295   microglia in the lumbar spine of SOD1^{G93A} mice. Furthermore, gliosis in the SOD1^{G93A} mice was

296   associated with a trend towards fewer motor neurons in the lumbar spine at day 90 of age (30

297   dpi), as measured by ChAT+ cells (**Supplemental Fig. 3**).

298

299   Additionally, RNA was isolated from the lumbar spine of both previously IAV infected and

300   uninfected SOD1^{G93A} mice at 90 days of age (30 dpi) and subjected to RNA sequencing to

301   identify differentially expressed genes. Gene set enrichment analysis (GSEA) revealed

302   significant upregulation in pathways associated with innate and adaptive immunity, lipid

303   metabolism, apoptotic pathways, and muscle dysfunction in previously IAV infected SOD1^{G93A}

304   mice compared to uninfected SOD1^{G93A} mice (**Fig 4D**). Specifically, pathways related to

305   inflammatory and immune responses were prominently elevated, indicating a robust immune

306   activation in the lumbar spine well after IAV infection was resolved. Overall, these results

307   suggest that prior acute viral infection potentiates gliosis in the lumbar spine and induction of

308   transcriptional programs relating to inflammation, immunity, and lipid and muscular

309   dysfunction.

310

311   **Inhibition of microglial activation during acute IAV infection protects SOD1^{G93A} mice from**

312   **accelerated disease progression.**

313

314   We have thus far demonstrated that a single acute infection event prior to onset of ALS clinical

315   signs accelerates ALS disease progression in SOD1^{G93A} mice, and resulted in elevated

316   inflammatory signatures and gliosis in the lumbar spine. Consequently, we next sought to

317   determine whether inhibiting this activation during acute infection could prevent ALS disease

318   acceleration. Minocycline is known to have anti-inflammatory properties and inhibit aberrant

319   microglial activation[41]. Importantly, minocycline has been shown to improve ALS outcomes in

320   transgenic SOD1 mice by inhibiting microglial activation[42]. To test whether inhibiting microglia

321   activation during acute infection prevents IAV-induced ALS acceleration, SOD1^{G93A} mice were

322   administered 50 mg/kg minocycline via intraperitoneal (i.p.) injection daily. Treatment was

323   initiated one day prior to infection (day 59 of age) and continued until 3 weeks post-infection

324   (day 81 of age) (**Fig. 5A**). Both minocycline treated and untreated mice infected with IAV

325   experienced similar kinetics of weight loss following infection, with weight loss peaking around

326   8 dpi (**Fig. 5B**), indicating that treatment did not alter acute disease kinetics in comparison to

327   controls. At 2 weeks post-infection, mice were assessed on the rotarod. SOD1^{G93A} mice

328   administered minocycline performed significantly better on the rotarod test with a significant

329   delay in minocycline treated mice reaching 50% of their initial fall time compared to untreated

330   mice infected with IAV (**Fig. 5C**). However, there were no observable differences in survival

331   due to ALS clinical sign progression between the two groups. The shape of the Kaplan-Meyer

332   curve alongside the rotarod data suggest that the benefits of minocycline may diminish upon

333   cessation of treatment (**Fig. 5D**). We next assessed levels of microglial activation in the lumbar

334   spine at the time of treatment cessation (day 81 of age – 3 weeks post-infection). Indeed, we

335   observed a trend towards decreased Iba1+ cells in minocycline treated SOD1^{G93A} mice infected

336   with IAV compared to those infected receiving vehicle control (**Fig. 5E**). Altogether, these

337   results indicate that inhibiting microglial activation during acute infection helps to prevent

338   infection-induced disease acceleration.

339

340   **Oseltamivir treatment during IAV infection protects SOD1^{G93A} mice from accelerated**

341   **disease progression.**

342

343   We have shown that prior IAV infection potentiates gliosis in lumbar spine of SOD1^{G93A} mice,

344   and that administering minocycline reduces IAV-induced glial activation resulting in subsequent

345   motor function improvements. We next examined the protective role of administering a direct-

346   acting antiviral on infection-induced ALS disease acceleration. Oseltamivir is a direct-acting

347   antiviral that prevents influenza illness by inhibiting the activity of neuraminidase on influenza

348   viruses[43]. To this end, SOD1^{G93A} mice were infected i.n. with a sublethal dose of IAV at day 60

349   of age and were subsequently administered 10 mg/kg oseltamivir phosphate via oral gavage

350   twice daily. Oseltamivir administration was initiated 1 dpi and continued for 7 consecutive days

351   (**Fig. 6A**). As expected, oseltamivir administration attenuated disease, reducing weight loss

352   following IAV infection compared to mice administered vehicle control (**Fig. 6B**). Additionally,

353   IAV-infected mice administered oseltamivir had better motor performance on the rotarod test

354   compared to infected mice that were administered vehicle control (**Fig. 6C**). However, similar to

355   minocycline treatment, this did not result in a significant lengthening of survival, though there

356   was a positive trend (**Fig. 6D**). Collectively, these data demonstrate the therapeutic benefit of

357   antiviral treatment in preventing accelerated ALS motor decline resulting from IAV infection.

358

359   **SARS-CoV-2 infection prior to ALS onset accelerates disease progression in SOD1^{G93A}**

360   **mice.**

361

362   Given the widespread global impact of COVID-19, we next sought to determine whether similar

363   ALS disease acceleration was observed in SOD1^{G93A} mice acutely infected with SARS-CoV-2.

364   To this end, SOD1^{G93A} mice were infected i.n. with a sublethal dose (10^5 PFU) of a mouse-

365   adapted SARS-CoV-2 (strain MA10) (**Fig. 7A**). We observed that SOD1^{G93A} mice infected with

366   SARS-CoV-2 had worse motor performance assessed through the inverted grip test (**Fig. 7B**).

367   However, in contrast to acute IAV infection, acute SARS-CoV-2 infection did not accelerate

368   time to endpoint due to ALS clinical signs faster than uninfected controls (**Fig. 7C**). Next to

369   assess SARS-CoV-2 infection disease kinetics in this model, SOD1^{G93A} mice were infected i.n.

370   with a sublethal dose of SARS-CoV-2. We observed no appreciable weight loss throughout the

371   course of infection (**Fig. 7D**), and in concordance with IAV infection, WT and SOD1^{G93A} mice

372   experience similar viral burden within the lungs (**Fig. 7E**). Taken together, these results suggest

373   that a sublethal SARS-CoV-2 infection during the pre-symptomatic stages of ALS significantly

374   accelerates motor decline.

375

376   **Discussion**

377

378   ALS remains an incurable disease and current treatments have relatively modest therapeutic

379   benefits. Tremendous efforts have been made to develop new treatments, however many clinical

380   trials have eventually failed to slow disease progression as measured by the ALSFRS-R[44,45]. The

381   immense heterogeneity of ALS is an important factor contributing to this lack of success, a

382   product of genetic and environmental factors[46]. Viral infections have long been associated with

383   ALS and other neurodegenerative diseases. However, most prior studies have been based on

384   observational studies that are correlative in nature. Additionally, these studies have largely

385   focused on chronic and neurotropic infections, as these are more easily detected in post-mortem

386   and serological analyses of ALS patients. Indeed, infections that occur and are resolved

387   throughout the life of an individual can have profound long-term impacts (e.g. "long COVID").

388   Importantly, the mechanism underlying viral-mediated potentiation of ALS disease progression

389   has been widely understudied. Our study demonstrates that a single, acute infection with

390   common pathogens, such as IAV and SARS-CoV-2, during the pre-symptomatic stages of

391   disease accelerates the progression of ALS in a murine model. Our work also suggests that

392   potentiation of aberrant inflammatory immune processes in the CNS may be a unifying

393   mechanism to explain why so many viruses with diverse biologies have been implicated in ALS.

394

395   Here, we used the SOD1^{G93A} model to explore the mechanisms through which viral infections

396   impact ALS disease. This is one of the most extensively characterized mouse models of ALS

397   with tractable disease features that closely resemble "classical" ALS[47,48]. Additionally, timing of

398   disease onset and rate of progression are predictable and have been widely documented, allowing

399   us to investigate whether infection during pre-symptomatic stages has an influence on disease

400   progression[48]. A mouse-adapted strain of IAV subtype H1N1 (PR8) and mouse-adapted SARS-

401   CoV-2 (strain MA10) were used as model pathogens due to their ubiquity. Importantly, previous

402   studies indicate that these particular isolates are not neuroinvasive, yet infection induces

403   signatures of neuroinflammation through peripheral perturbations[19,49,50].

404

405   We found that a sublethal i.n. infection with IAV at day 60 of age resulted in poorer motor

406   function and significant acceleration of disease relative to uninfected SOD1^{G93A} mice. Disease

407   acceleration was also observed in SOD1^{G93A} mice infected with SARS-CoV-2. This acceleration

408   occurred despite clearance of the virus, as no detectable virus was found in the lungs or brains of

409   infected WT and SOD1^{G93A} mice following infection resolution at 14 dpi[19]. Furthermore, we

410   observed no differences in the dynamics of acute infection experienced by WT and SOD1^{G93A}

411   mice following IAV and SARS-CoV-2, with both genotypes demonstrated similar weight loss

412   trajectories and viral burden in the lungs following infection. This suggests that individuals at

413   risk of developing ALS may not be inherently more susceptible to infection prior to onset of

414   clinical disease.

415

416   Neuroinflammation is a well-established feature of ALS and other related neurodegenerative

417   diseases, like Parkinson's Disease and Alzheimer's Disease. Indeed, as we and others have

418   shown, many genes associated with ALS have important roles in regulating innate and adaptive

419   immune responses to infection[51–53]. ALS disease progression is correlated with elevated levels of

420   soluble pro-inflammatory mediators in the peripheral blood and CSF, and there is evidence of

421   substantial cross-talk between the periphery and CNS[26,27]. Interestingly, we observed elevated

422   levels of pro-inflammatory cytokines/chemokines in the lungs and brains of infected WT and

423   SOD1[G93A] mice at 4 dpi that remained elevated 30 dpi, well after the initial infection had been

424   resolved. This suggests long-term neuroinflammation can be caused by acute infection

425   originating from peripheral responses. To distinguish the relative contribution of infection-

426   induced immunity on ALS acceleration relative to that of virus replication itself, inactivated IAV

427   was administered through i.m. or i.n. inoculation. We observed that i.m. administration in the

428   quadriceps resulted in accelerated ALS disease progression of SOD1[G93A] mice relative to those

429   administered vehicle control. However, this was not observed when inactivated IAV was i.n.

430   administered. Taken together, our findings show that inflammation induced by viral exposure

431   (and not exclusively the direct effects of viral replication alone), are important for accelerating

432   ALS disease progression. Additionally, the location in which inflammation is generated is

433   critical. Systemic inflammation and inflammation generated in disease susceptible tissue, such as

434   the hindlimbs in the SOD1^{G93A} model, appears to be especially deleterious to these mice,

435   whereas inflammation localized in tissues distal from the sites of disease, such as the lungs, did

436   not accelerate progression.

437

438   To gain further mechanistic insight, immunohistochemical analysis of the lumbar spine provided

439   evidence of elevated astrocyte and microglial activation levels in previously infected SOD1^{G93A}

440   mice compared to control mice at day 90 of age (30 dpi). Given the reported importance of glial

441   cells in ALS pathophysiology, the observation that acute infection results in sustained gliosis,

442   long after the infection is cleared, provides a compelling mechanism through which these

443   infections potentiate ALS. The immunohistochemical findings were further corroborated through

444   bulk RNA sequencing of the lumbar spinal cord of previously IAV infected and control

445   SOD1^{G93A} mice. GSEA revealed significantly enriched transcripts for pathways relating to

446   inflammation, immunity, lipid and muscle dysregulation and apoptosis in IAV infected

447   SOD1^{G93A} mice. As previously mentioned, soluble pro-inflammatory mediators and the induction

448   of innate and adaptive immunity are positively correlated with ALS progression. However,

449   interestingly, enrichment of lipid dysregulation and apoptotic pathways suggests additional

450   changes in bioenergetics and intrinsic cellular processes in the lumbar spine following IAV

451   infection. Indeed, dysregulated lipid profiles and apoptotic signaling have been observed in ALS

452   patients[54–56]. Notably, gene sets related to muscle dysfunction and weakness were upregulated in

453   IAV infected SOD1^{G93A} mice, indicating exacerbated neuromuscular impairment characteristic of

454   this ALS model. Muscle weakness and atrophy are primary symptoms of ALS, and their

455   exacerbation following viral infection suggests a potential interaction between acute peripheral

456   IAV infection and neuromuscular health[57].

457

458   Given our findings that acute viral infection accelerates disease, presumably via potentiation of

459   pathogenic immune responses in the CNS, we sought to determine the therapeutic potential of

460   two separate approaches: chemically inhibiting microglial activation, and treating acute viral

461   infection using antivirals. We found that minocycline and OSLT treatment improved

462   performance of SOD1^{G93A} mice on the rotarod. This suggests that acute treatment is efficacious

463   but must likely be sustained following infection in order to extend survival (since we observed

464   the resumption of accelerated disease upon treatment cessation). Indeed, prior studies showing

465   efficacy of antivirals and immunomodulatory drugs in pre-clinical models have maintained

466   treatment for the duration of the disease[11,58–60].

467

468   The data presented here demonstrates that a single sublethal infection with common, acute

469   viruses exacerbate ALS disease. These results also underscore inherent difficulties in conducting

470   these types of studies in humans. In our model, were no observable differences in susceptibility

471   to, or severity of acute viral infection when comparing WT and SOD1^{G93A} mice. Furthermore,

472   acceleration of disease was not evident until several weeks after the acute infections had been

473   cleared. These types of "hit-and-run" mechanisms are inherently challenging to study in

474   epidemiological contexts – especially for ubiquitous pathogens wherein differences in

475   seroprevalence would not be expected. Elegant recent work using data from European biobanks,

476   highlighted extensive associations between infections and many neurodegenerative diseases,

477   including ALS, even 15 years following an exposure[17]. Here, we build on those studies and

478   provide mechanistic insight that may explain how and why pathogens with inherently different

479   biologies all contribute to neurodegenerative disease – namely, through their shared propensity

480   to elicit inflammatory immune responses. To our knowledge, this is the first study investigating

481   whether a direct causal relationship exists with acute viral infections (particularly non-

482   neurotropic infections), and ALS progression. This should set the stage for additional studies in

483   human cohorts at risk for developing ALS.

484

485   **Limitations**

486

487   For practical reasons, our studies were limited to the SOD1^{G93A} mouse model, which is one of the

488   few ALS models that recapitulates key features of neuromuscular disease with predictable and

489   tractable kinetics. In the future, it would be interesting to validate that our findings extend to

490   other ALS models with distinct genetic backgrounds (most of which do not show a

491   neuromuscular phenotype, but may demonstrate features consistent for frontotemporal dementia,

492   for example). Likewise, it would be interesting to determine whether infection could serve as a

493   trigger for ALS in a model wherein animals do not spontaneously develop disease. However, a

494   suitable "inducible" model of ALS has yet to be developed, to our knowledge.

495

496   **Materials and Methods**

497

498   *Animal colony and ethics statement*

499   All mouse experiments were approved by the McMaster University Animal Research Ethics

500   Board. SOD1 Tg mice expressing the G93A mutation, raised on the B6SJL-

501   TgN(SOD1*G93A)1Gur background (SOD1^{G93A}), and wildtype BL6SJL (WT) mice were

502   purchased from the Jackson Laboratory. Mice were maintained on a 12 hour light/dark cycle and

503   low-fat dietary chow and water was provided *ad libitum*. Breeding pairs consisted of male

504   SOD1^{G93A} mice and female WT mice, and mice were bred up to the second generation. Litters

505   were weaned at 21 days of age and housed at a maximum of five mice per cage. All experimental

506   mice were age-matched.

507

508   *Viruses and Cells*

509   Influenza A/Puerto Rico/8/1934/H1N1 (PR8) was propagated in 10 day-old specific-pathogen-

510   free embryonated chicken eggs (Canadian Food Inspection Agency)[61]. Viral stock concentrations

511   were quantified by performing plaque assay on Madin-Darby Canine Kidney (MDCK) cells

512   (ATCC, VA, USA). SARS-CoV-2 MA10 was kindly provided by Dr. Ralph Baric[62]. MDCKs

513   and VeroE6 cells (ATCC, VA, USA) were maintained in Dulbecco's minimal essential media

514   (DMEM) (Gibco) supplemented with 1 X GlutaMAX^{TM} supplement (Gibco), 10% heat

515   inactivated fetal bovine serum (FBS) (Gibco), 100 U/mL penicillin and 100 µg/mL streptomycin

516   (Gibco), and 1% of 1 M HEPES (ThermoFisher) at 37°C and 5% CO_2. Mouse embryonic

517   fibroblasts (MEFs) were isolated from embryos 13.5 days post-conception as previously

518   described[63]. MEFs were maintained in DMEM supplemented with 1 X GlutaMAX^{TM}

519   supplement, 15% FBS, and 100 U/mL penicillin and 100 µg/mL streptomycin and incubated at

520   37°C and 5% CO_2.

521

522   *IAV and SARS-CoV-2 Infection*

523   WT and SOD1^{G93A} mice were anesthetized using isoflurane and infected with IAV i.n. in a 40

524   µL inoculum of PBS. Mice were infected with 300 plaque forming units (PFU) of IAV, equating

525   to a 0.1 median lethal dose (LD$_{50}$) infection. SARS-CoV-2 infections were performed using a

526 mouse-adapted strain of SARS-CoV-2 MA10. Mice were anesthetized using isoflurane and

527 infected with SARS-CoV-2 MA10 i.n. at a dose of 10^5 PFU. Weight loss, lethargy, and general

528 body condition were monitored following infection for up to 2 weeks post-infection. Endpoint

529 due to IAV- and SARS-CoV-2-associated mortality was defined as mice reaching 80% of their

530 pre-infection weight.

531

532 *Cytokine and Chemokine Analysis*

533 Evaluation of cytokine and chemokine induction in the lungs, brain, and lumbar spinal cord were

534 performed through a mouse 32-plex cytokine/chemokine array (MD32) (Eve Technologies,

535 Alberta, Canada).

536

537 *IAV Inactivation*

538 100 X inactivation solution (0.925% formaldehyde in PBS) (Anachemia) was combined with 4.2

539 mg/mL of purified IAV suspension to a final concentration of 1 X inactivation solution. Samples

540 were incubated at 4°C on constant rotation for 72 hours, followed by storage at -80°C.

541

542 *Inactivated IAV Administration*

543 WT and SOD1^{G93A} mice were administered 50 µg of formaldehyde-inactivated IAV in a 100 µL

544 inoculum via i.m. injection into the quadricep muscle, and. i.n. administration was performed

545 with a 40 µL inoculum of 50 µg of formaldehyde-inactivated IAV.

546

547 *Rotarod Test*

548   Motor performance and general coordination was measured using the rotarod test (Panlab,

549   Harvard Apparatus, Holliston, MA, USA). The rotarod was set to acceleration mode (4 rpm to 15

550   rpm in 60 s, or 0.2 rpm/s) for a maximum rotation speed of 15 rpm. WT and SOD1^{G93A} mice

551   were tested for a maximum of 180 seconds and the latency for falling off the apparatus was

552   recorded. Mice were assessed once weekly until they were unable to support themselves on the

553   apparatus, with the average of six trials being used.

554

555   *ALS Clinical Sign Assessment and Endpoint Monitoring*

556   At day 120 of age, mice were monitored daily until reaching endpoint due to ALS clinical signs.

557   Mice were assessed based on a 4-point neurological scoring system. Score 0: full extension of

558   hind-limbs when suspended by the tail, Score 1: collapse or partial collapse of the hind-limbs

559   and/or trembling of the hind-limbs when suspended by the tail, Score 2: Toe curling during

560   locomotion, Score 3: paralysis of one or both of the hind-limbs, Score 4: unable to right

561   themselves within 30 s of being placed on either side. Endpoint was defined as mice reaching a

562   neurological score of 4.

563

564   *IAV Plaque Assay*

565   MDCK cells were seeded in a 6-well plate at a density of 6.5 x 10^5 cells per well and incubated

566   for 48 hours at 37 ºC in 5 % CO2. Following incubation, samples were serially diluted in 1 X

567   Minimum Essential Media (MEM), 1 X GlutaMAX^{TM} supplement, 1.5 % sodium bicarbonate,

568   200 mM HEPES, 1 X MEM Vitamin Solution, 1 X MEM Amino Acid Solution, 2 mg/mL

569   penicillin/streptomycin, 7 % BSA). Cells were infected for 1 hour at 37 ºC in 5 % CO_2. Cells

570   were subsequently overlayed with 1 % (m/v) agar bacteriological combined with one part 2 X

571   MEM, 0.01 % DEAE-Dextran, 1 µg/mL N-p-Tosyl-L-phenylalanine chloromethyl ketone

572   (TPCK)-treated trypsin and plates were incubated at 37 ºC in 5 % CO_2 for 48 hours. Cells were

573   fixed with 3.7 % formaldehyde diluted in PBS for 30 min at RT and stained with crystal violet.

574

575   *IAV Growth Curves*

576   WT and SOD1^{G93A} MEFs were infected with IAV at a multiplicity of infection (MOI) of 3.

577   Supernatant was collected at 0, 2, 4, 8, 12, 24, and 48 hours post-infection and viral titres were

578   assessed using plaque assays on MDCK cells. For *in vivo* studies, WT and SOD1^{G93A} mice were

579   infected with 300 PFU of IAV i.n. and lungs were collected in serum-free DMEM, and

580   homogenized using the Bullet Blender Gold High-Throughput Bead Mill Homogenizer (Next

581   Advance). Viral titres from lung homogenates were determined via plaque assay on MDCK

582   cells.

583

584   *Antiviral Gene Expression Quantification and Cytokine Analysis*

585   WT and SOD1^{G93A} MEFs were plated and stimulated with UV-inactivated IAV at an MOI of 10

586   equivalent and supernatant was collected at 0, 4, 8, and 24 hours post-stimulation. For gene

587   expression quantification, RNA from cell lysates was isolated using the RNeasy kit (Qiagen) and

588   1 µg of complimentary DNA was synthesized using the Maxima First Strand cDNA Synthesis

589   kit, according to manufacturers instructions (Thermo Fisher Scientific). Gene expression levels

590   were assessed using SensiFAST SYBR reaction kit (Bioline Reagents Ltd.) for quantitative real-

591   time PCR (qRT-PCR). For cytokine analysis, supernatant from stimulated MEFs were collected

592   at 0, 4, 8, and 24 h post-stimulation. For *in-vivo* studies, mice were infected with 300 PFU IAV

593   i.n. and lung and brain homogenates were harvested in PBS containing Pierce Protease Inhibitor

594   (Thermo Fisher Scientific) at 4- and 30- days post-infection. Cytokine levels were assessed using

595   a 32-plex mouse cytokine/chemokine array (EVE Technologies Corp., Calgary, AB, Canada).

596

597   *Fluorescent Immunohistochemistry*

598   Spinal cord sections were isolated using hydraulic extrusion as previously described, with slight

599   modifications[64]. Briefly, mice were anesthetized and transcardially perfused with PBS. The

600   spinal cord was removed and cut immediately distal to the 13th rib to isolate the lumbar spine.

601   The lumbar spinal cord was hydraulically removed from the vertebrae using 5 mL of PBS and

602   stored in 3.7 % PFA for 72 hours. Subsequently, samples were sliced 5 µm thick and mounted

603   onto paraffin. Sections were deparaffinized with xylene and subsequently dehydrated using

604   decreasing ethanol concentrations of 100%, 95%, 95%, 75%, and 75%, for 5 min at each step.

605   Slices were then rehydrated in H_2O for 5 min. Antigen retrieval was performed with 1 X citrate

606   buffer (Abcam) for 20 min at 95°C. Thereafter, slices were washed 3 times with PBS-T (0.1%

607   Tween 20, Sigma Aldrich). Slices were permeabilized using 0.2 % Triton™ X-100 diluted in

608   PBS-T for 20 min at RT, and then washed 3 times with PBS-T. Following permeabilization,

609   slices were blocked with 10% normal goat serum (Abcam) and 1% BSA diluted in PBS for 1

610   hour at RT. Spinal cord slices were incubated with primary antibodies overnight at 4°C. Primary

611   antibodies included: Iba1 [1:300] (Abcam), GFAP [1:400] (Abcam), ChAT [1:100] (Abcam).

612   Slices were then washed 3 times with PBS-T and probed with compatible AlexaFluor-conjugated

613   secondary antibodies at a 1:1000 dilution (Invitrogen), washed 3 times, and mounted with

614   EverBrite mounting medium (Biotium Inc.). Images were taken with the Zeiss Imager M2

615   microscope.

616

617 *Minocycline and Oseltamivir Treatment*

618 Minocycline hydrochloride (Sigma-Aldrich) was dissolved in PBS and administered

619 intraperitoneally (i.p.) once daily to SOD1^{G93A} at a dose of 50 mg/kg beginning one day prior to

620 infection (day 59 of age) for a duration of three weeks following infection (day 81 of age). Mice

621 were monitored for weight loss, assessed on the rotarod, and monitored until reaching endpoint

622 due to ALS clinical signs. For therapeutic oseltamivir treatment, mice were infected at day 60 of

623 age and treated twice daily with 10 mg/kg oseltamivir phosphate (Toronto Research Chemicals,

624 O701000) via oral gavage for 7 consecutive days starting at 1 dpi. Mice were monitored for

625 weight loss, assessed on the rotarod, and monitored until reaching endpoint due to ALS clinical

626 signs.

627

628 *RNA Sequencing*

629 Lumbar spinal cord was extracted and flash frozen in liquid nitrogen. Once frozen, samples

630 within a cryotube were disrupted using a pestle and homogenized by pipetting with 600 µL of

631 RLT buffer (Qiagen). Homogenized samples were then transferred to a Qiashredder spin column

632 (Qiagen), and the flowthrough was subsequently spun in a gDNA eliminator column (Qiagen).

633 Equal volume of 70% ethanol was added and RNA isolation was carried out as per the RNeasy

634 instruction manual (Qiagen). Sample libraries were prepared using the NEBNext Ultra^{TM} II

635 Directional RNA Library Prep Kit for Illumina (New England Biolabs) and cDNA libraries were

636 sequenced using an Illumina HiSeq machine (2x50 bp sequence reads). The reads were trimmed

637 using TrimGalore and then aligned with GRCm39 reference using STAR[65]. Next, the reads were

638 counted by using HTSeq count[66]. Genes, showing low levels of expression were removed using

639 EdgeR package in R, resulting in 12,503 genes[67]. Counts for these remaining genes were

640 normalized with TMM normalization method and then transformed using voom

641 transformation[68,69]. The limma package in R was used to identify genes differentially expressed

642 between the infected and the uninfected groups of each genotype[70]. For differential expression

643 analysis, corrected p-values < 0.05 were considered to be significant. Gene Set Enrichment

644 Analysis (GSEA) was performed to compare WT and SOD1^{G93A} IAV infected to their uninfected

645 counterparts respectively using C2 canonical pathways and C5 GO collections[71]. Enrichment

646 with corrected p-value < 0.1 was considered to be significant. GSEA results were shown using

647 Enrichment Maps in Cytoscape environment and barplots created in R[72]. Additional results were

648 visualized in PCA plot using rgl package in R.

649

650 *Statistical Analysis*

651 All data and figures were generated, and statistical analyses were performed using GraphPad

652 Prism (GraphPad Software v.10., La Jolla, CA, USA).

653
654

655 **Key resources table**

656

REAGENT or RESOURCE	SOURCE	IDENTIFIER
Antibodies		
Iba1	Abcam	Cat#178846
GFAP	Abcam	Cat#ab7260
ChAT	Abcam	Cat#ab181023
Alexa Fluor™ 488 goat anti-rabbit IgG (H+L) secondary antibody	Invitrogen	Cat#A11008
Bacterial and virus strains		
A/Puerto Rico/8/1934 H1N1 (PR8)	Gift from Dr. Peter Palese, Icahn School of Medicine at Mount Sinai, NY	NCBI taxon ID#211044
SARS-CoV-2 MA10	Gift from Dr. Ralph Baric, University of North Carolina at Chapel Hill, NC	Cat#NR-55329 Leist et al., 2020

Biological samples		
Chemicals, peptides, and recombinant proteins		
DMEM	Gibco	Cat#11965092
Penicillin-Streptomycin	Gibco	Cat#15140122
GlutaMAX™ Supplement	Gibco	Cat#35050061
Heat Inactivated FBS	Gibco	Cat#12484028
HEPES	ThermoFisher Scientific	Cat#15630080
MEM	Sigma-Aldrich	Cat#M0275
BSA	Sigma-Aldrich	Cat#A8412
Sodium Bicarbonate Solution	Sigma-Aldrich	Cat#S8761
MEM Vitamin Solution	Gibco	Cat#11120052
MEM Amino Acids Solution	Gibco	Cat#11130051
Trypsin-EDTA	Gibco	Cat#15400054
Trypsin treated with N-tosyl-L-phenylalanine chloromethyl ketone (TPCK)	Sigma-Aldrich	Cat#4370285
Oseltamivir Phosphate	Toronto Research Chemicals	Cat#O701000
Hoechst-33342	Invitrogen	Cat#H3570
Triton™ X-100	ThermoFisher Scientific	Cat#BP151-500
Antigen Retrieval Buffer (100X Citrate Buffer pH 6.0)	Abcam	Cat#ab93678
Xylenes	Sigma Aldrich `	Cat# 534056
Formaldehyde 37%	Anachemia	Cat#41860-360
EverBrite Mounting Media	Biotium	Cat#23001
Agar Bacteriological (Agar NO.1)	Oxoid	Cat#LP0011
Pierce™ Protease Inhibitor Tablets, EDTA-free	ThermoFisher Scientific	Cat#A32965
Normal Goat Serum	Abcam	Cat#ab7481
Minocycline hydrochloride	Sigma Aldrich	Cat#M9511
Tween 20	Sigma Aldrich	Cat#P9416
Critical commercial assays		
RNeasy Mini Kit	Qiagen	Cat#74106
Maxima First Strand cDNA Synthesis Kit for RT-qPCR	ThermoFisher Scientific	Cat#K1641
SensiFAST SYBR Hi-ROX Kit	Meridian Bioscience	Cat#BIO-92005
NEBNext Ultra™ II Directional RNA Library Prep Kit for Illumina	New England Biolabs	Cat#E7760L
Experimental models: Cell lines		
Mouse embryonic fibroblasts	This study	N/A
MDCK.2	ATCC	Cat#CRL-2936
Vero E6	ATCC	Cat#CRL-1586

Experimental models: Organisms/strains		
Mouse:B6SJL-Tg(SOD1*G93A)1Gur/J	The Jackson Laboratory	JAX#002726 RRID:IMSR_JAX:002726
Mouse: B6SJLF1/J	The Jackson Laboratory	JAX#100012 RRID: IMSR_JAX:100012
Specific-pathogen-free (SPF) chicken eggs	Canadian Food Inspection Agency (CFIA)	N/A
Oligonucleotides		
IFITM3 Forward Primer (5' – GACAGCCCCCAAACTACGAA – 3')	Invitrogen	N/A
IFITM3 Reverse Primer (5' – ATTGAACAGGGACCAGACCAC – 3')	Invitrogen	N/A
DDX58 Forward Primer (5' – ATGTGCCCCTACTGGTTGTG – 3')	Invitrogen	N/A
DDX58 Reverse Primer (5' – CCCCAGAAATGCTCGCAATG – 3')	Invitrogen	N/A
IFIT1 Forward Primer (5' – CTTTACAGCAACCATGGGAGAGA – 3')	Invitrogen	N/A
IFIT1 Reverse Primer (5' – TGATGTCAAGGAACTGGACCTG – 3')	Invitrogen	N/A
18S Forward Primer (5' – GTAACCCGTTGAACCCCATT – 3')	Invitrogen	N/A
18S Reverse Primer (5' – CCATCCAATCGGTAGTAGCG – 3')	Invitrogen	N/A
Software and algorithms		
Graphpad Prism, version 10		

657

658

659

660 **Acknowledgement:**

661

669
670

671

Author Contributions:

673

674   Conceptualization, A.M., J.M., B.C., M.S.M.; methodology, A.M., J.M., B.C., M.S.M.; formal

675   analysis, A.M., J.M., B.C., A.D.G.; M.S.M.; investigation, A.M., J.M., B.C., D.C., M.R.D, S.A.,

676   J.C.A., A.T.C, V.S., A.Z., H.D.S., M.L., Y.K., K.M., M.S.M.; writing, A.M., S.A., J.M., M.S.M.;

677   supervision, M.S.M.

678
Data and Materials Availability:

680

681   All data, code, and materials reported in this article will be shared by the lead contact upon

682   request.

683
Declaration of Interests:
685
686
687   All authors declare no competing interest.
688
689
690
References
692
693

1. Kanouchi, T., Ohkubo, T., and Yokota, T. (2012). Can regional spreading of amyotrophic lateral sclerosis motor symptoms be explained by prion-like propagation? J Neurol Neurosurg Psychiatry *83*, 739–745. https://doi.org/10.1136/jnnp-2011-301826.

2. Bäumer, D., Talbot, K., and Turner, M.R. (2014). Advances in motor neurone disease. J R Soc Med *107*, 14–21. https://doi.org/10.1177/0141076813511451.

3. van Es, M.A., Hardiman, O., Chio, A., Al-Chalabi, A., Pasterkamp, R.J., Veldink, J.H., and van den Berg, L.H. (2017). Amyotrophic lateral sclerosis. Lancet *390*, 2084–2098. https://doi.org/10.1016/S0140-6736(17)31287-4.

4. Swinnen, B., and Robberecht, W. (2014). The phenotypic variability of amyotrophic lateral sclerosis. Nat Rev Neurol *10*, 661–670. https://doi.org/10.1038/nrneurol.2014.184.

5. Turner, M.R., Hardiman, O., Benatar, M., Brooks, B.R., Chio, A., de Carvalho, M., Ince, P.G., Lin, C., Miller, R.G., Mitsumoto, H., et al. (2013). Controversies and priorities in amyotrophic lateral sclerosis. Lancet Neurol *12*, 310–322. https://doi.org/10.1016/S1474-4422(13)70036-X.

6. Ingre, C., Roos, P.M., Piehl, F., Kamel, F., and Fang, F. (2015). Risk factors for amyotrophic lateral sclerosis. Clin Epidemiol *7*, 181–193. https://doi.org/10.2147/CLEP.S37505.

7. Xue, Y.C., Feuer, R., Cashman, N., and Luo, H. (2018). Enteroviral Infection: The Forgotten Link to Amyotrophic Lateral Sclerosis? Front Mol Neurosci *11*, 63. https://doi.org/10.3389/fnmol.2018.00063.

8. Celeste, D.B., and Miller, M.S. (2018). Reviewing the evidence for viruses as environmental risk factors for ALS: A new perspective. Cytokine *108*, 173–178. https://doi.org/10.1016/j.cyto.2018.04.010.

9. Fung, G., Shi, J., Deng, H., Hou, J., Wang, C., Hong, A., Zhang, J., Jia, W., and Luo, H. (2015). Cytoplasmic translocation, aggregation, and cleavage of TDP-43 by enteroviral proteases modulate viral pathogenesis. Cell Death Differ *22*, 2087–2097. https://doi.org/10.1038/cdd.2015.58.

10. Mackenzie, I.R.A., Bigio, E.H., Ince, P.G., Geser, F., Neumann, M., Cairns, N.J., Kwong, L.K., Forman, M.S., Ravits, J., Stewart, H., et al. (2007). Pathological TDP-43 distinguishes sporadic amyotrophic lateral sclerosis from amyotrophic lateral sclerosis with SOD1 mutations. Ann Neurol *61*, 427–434. https://doi.org/10.1002/ana.21147.

11. Xue, Y.C., Liu, H., Mohamud, Y., Bahreyni, A., Zhang, J., Cashman, N.R., and Luo, H. (2022). Sublethal enteroviral infection exacerbates disease progression in an ALS mouse model. J Neuroinflammation *19*, 16. https://doi.org/10.1186/s12974-022-02380-7.

12. Douville, R.N., and Nath, A. (2014). Human endogenous retroviruses and the nervous system. Handb Clin Neurol *123*, 465–485. https://doi.org/10.1016/B978-0-444-53488-0.00022-5.

13. Li, W., Lee, M.-H., Henderson, L., Tyagi, R., Bachani, M., Steiner, J., Campanac, E., Hoffman, D.A., von Geldern, G., Johnson, K., et al. (2015). Human endogenous retrovirus-K contributes to motor neuron disease. Sci Transl Med *7*, 307ra153. https://doi.org/10.1126/scitranslmed.aac8201.

14. Pasternack, N., Doucet-O'Hare, T., Johnson, K., NYGC Consortium, Paulsen, O., and Nath, A. (2024). Endogenous retroviruses are dysregulated in ALS. iScience *27*, 110147. https://doi.org/10.1016/j.isci.2024.110147.

15. Garcia-Montojo, M., Fathi, S., Norato, G., Smith, B.R., Rowe, D.B., Kiernan, M.C., Vucic, S., Mathers, S., van Eijk, R.P.A., Santamaria, U., et al. (2021). Inhibition of

740   HERV-K (HML-2) in amyotrophic lateral sclerosis patients on antiretroviral therapy. J
741   Neurol Sci *423*, 117358. https://doi.org/10.1016/j.jns.2021.117358.

742   16.   Gold, J., Rowe, D.B., Kiernan, M.C., Vucic, S., Mathers, S., van Eijk, R.P.A., Nath, A.,
743   Garcia Montojo, M., Norato, G., Santamaria, U.A., et al. (2019). Safety and tolerability of
744   Triumeq in amyotrophic lateral sclerosis: the Lighthouse trial. Amyotroph Lateral Scler
745   Frontotemporal Degener *20*, 595–604. https://doi.org/10.1080/21678421.2019.1632899.

746   17.   Levine, K.S., Leonard, H.L., Blauwendraat, C., Iwaki, H., Johnson, N., Bandres-Ciga, S.,
747   Ferrucci, L., Faghri, F., Singleton, A.B., and Nalls, M.A. (2023). Virus exposure and
748   neurodegenerative disease risk across national biobanks. Neuron *111*, 1086-1093.e2.
749   https://doi.org/10.1016/j.neuron.2022.12.029.

750   18.   Bouvier, N.M., and Palese, P. (2008). The biology of influenza viruses. Vaccine *26 Suppl*
751   *4*, D49-53. https://doi.org/10.1016/j.vaccine.2008.07.039.

752   19.   Hosseini, S., Wilk, E., Michaelsen-Preusse, K., Gerhauser, I., Baumgärtner, W., Geffers,
753   R., Schughart, K., and Korte, M. (2018). Long-Term Neuroinflammation Induced by
754   Influenza A Virus Infection and the Impact on Hippocampal Neuron Morphology and
755   Function. J Neurosci *38*, 3060–3080. https://doi.org/10.1523/JNEUROSCI.1740-17.2018.

756   20.   Taquet, M., Geddes, J.R., Husain, M., Luciano, S., and Harrison, P.J. (2021). 6-month
757   neurological and psychiatric outcomes in 236 379 survivors of COVID-19: a
758   retrospective cohort study using electronic health records. Lancet Psychiatry *8*, 416–427.
759   https://doi.org/10.1016/S2215-0366(21)00084-5.

760   21.   Stefanou, M.-I., Palaiodimou, L., Bakola, E., Smyrnis, N., Papadopoulou, M., Paraskevas,
761   G.P., Rizos, E., Boutati, E., Grigoriadis, N., Krogias, C., et al. (2022). Neurological
762   manifestations of long-COVID syndrome: a narrative review. Ther Adv Chronic Dis *13*,
763   20406223221076890. https://doi.org/10.1177/20406223221076890.

764   22.   Meinhardt, J., Radke, J., Dittmayer, C., Franz, J., Thomas, C., Mothes, R., Laue, M.,
765   Schneider, J., Brünink, S., Greuel, S., et al. (2021). Olfactory transmucosal SARS-CoV-2
766   invasion as a port of central nervous system entry in individuals with COVID-19. Nat
767   Neurosci *24*, 168–175. https://doi.org/10.1038/s41593-020-00758-5.

768   23.   Silva, J., Patricio, F., Patricio-Martínez, A., Santos-López, G., Cedillo, L., Tizabi, Y., and
769   Limón, I.D. (2022). Neuropathological Aspects of SARS-CoV-2 Infection: Significance
770   for Both Alzheimer's and Parkinson's Disease. Front Neurosci *16*, 867825.
771   https://doi.org/10.3389/fnins.2022.867825.

772   24.   Merello, M., Bhatia, K.P., and Obeso, J.A. (2021). SARS-CoV-2 and the risk of
773   Parkinson's disease: facts and fantasy. Lancet Neurol *20*, 94–95.
774   https://doi.org/10.1016/S1474-4422(20)30442-7.

775   25.   McCauley, M.E., and Baloh, R.H. (2019). Inflammation in ALS/FTD pathogenesis. Acta
776   Neuropathol *137*, 715–730. https://doi.org/10.1007/s00401-018-1933-9.

777   26.   Beers, D.R., Zhao, W., Neal, D.W., Thonhoff, J.R., Thome, A.D., Faridar, A., Wen, S.,
778   Wang, J., and Appel, S.H. (2020). Elevated acute phase proteins reflect peripheral
779   inflammation and disease severity in patients with amyotrophic lateral sclerosis. Sci Rep
780   *10*, 15295. https://doi.org/10.1038/s41598-020-72247-5.

781   27.   Liu, Z., Cheng, X., Zhong, S., Zhang, X., Liu, C., Liu, F., and Zhao, C. (2020). Peripheral
782   and Central Nervous System Immune Response Crosstalk in Amyotrophic Lateral
783   Sclerosis. Front Neurosci *14*, 575. https://doi.org/10.3389/fnins.2020.00575.

784   28.   Nayak, J., Hoy, G., and Gordon, A. (2021). Influenza in Children. Cold Spring Harb
785   Perspect Med *11*, 1–17. https://doi.org/10.1101/cshperspect.a038430.

786   29.   Ruf, B.R., and Knuf, M. (2014). The burden of seasonal and pandemic influenza in infants
787   and children. Eur J Pediatr *173*, 265–276. https://doi.org/10.1007/s00431-013-2023-6.
788   30.   Meade, P., Kuan, G., Strohmeier, S., Maier, H.E., Amanat, F., Balmaseda, A., Ito, K.,
789   Kirkpatrick, E., Javier, A., Gresh, L., et al. (2020). Influenza Virus Infection Induces a
790   Narrow Antibody Response in Children but a Broad Recall Response in Adults. mBio *11*.
791   https://doi.org/10.1128/mBio.03243-19.
792   31.   Turner, B.J., and Talbot, K. (2008). Transgenics, toxicity and therapeutics in rodent
793   models of mutant SOD1-mediated familial ALS. Prog Neurobiol *85*, 94–134.
794   https://doi.org/10.1016/j.pneurobio.2008.01.001.
795   32.   Düsedau, H.P., Steffen, J., Figueiredo, C.A., Boehme, J.D., Schultz, K., Erck, C., Korte,
796   M., Faber-Zuschratter, H., Smalla, K.-H., Dieterich, D., et al. (2021). Influenza A Virus
797   (H1N1) Infection Induces Microglial Activation and Temporal Dysbalance in
798   Glutamatergic Synaptic Transmission. mBio *12*, e0177621.
799   https://doi.org/10.1128/mBio.01776-21.
800   33.   Decout, A., Katz, J.D., Venkatraman, S., and Ablasser, A. (2021). The cGAS-STING
801   pathway as a therapeutic target in inflammatory diseases. Nat Rev Immunol *21*, 548–569.
802   https://doi.org/10.1038/s41577-021-00524-z.
803   34.   Yu, C.-H., Davidson, S., Harapas, C.R., Hilton, J.B., Mlodzianoski, M.J.,
804   Laohamonthonkul, P., Louis, C., Low, R.R.J., Moecking, J., De Nardo, D., et al. (2020).
805   TDP-43 Triggers Mitochondrial DNA Release via mPTP to Activate cGAS/STING in
806   ALS. Cell *183*, 636-649.e18. https://doi.org/10.1016/j.cell.2020.09.020.
807   35.   Tan, H.Y., Yong, Y.K., Xue, Y.C., Liu, H., Furihata, T., Shankar, E.M., and Ng, C.S.
808   (2022). cGAS and DDX41-STING mediated intrinsic immunity spreads intercellularly to
809   promote neuroinflammation in SOD1 ALS model. iScience *25*, 104404.
810   https://doi.org/10.1016/j.isci.2022.104404.
811   36.   Rosário-Ferreira, N., Preto, A.J., Melo, R., Moreira, I.S., and Brito, R.M.M. (2020). The
812   Central Role of Non-Structural Protein 1 (NS1) in Influenza Biology and Infection. Int J
813   Mol Sci *21*. https://doi.org/10.3390/ijms21041511.
814   37.   Van Harten, A.C.M., Phatnani, H., and Przedborski, S. (2021). Non-cell-autonomous
815   pathogenic mechanisms in amyotrophic lateral sclerosis. Trends Neurosci *44*, 658–668.
816   https://doi.org/10.1016/j.tins.2021.04.008.
817   38.   Boillée, S., Yamanaka, K., Lobsiger, C.S., Copeland, N.G., Jenkins, N.A., Kassiotis, G.,
818   Kollias, G., and Cleveland, D.W. (2006). Onset and progression in inherited ALS
819   determined by motor neurons and microglia. Science *312*, 1389–1392.
820   https://doi.org/10.1126/science.1123511.
821   39.   Yamanaka, K., Chun, S.J., Boillee, S., Fujimori-Tonou, N., Yamashita, H., Gutmann,
822   D.H., Takahashi, R., Misawa, H., and Cleveland, D.W. (2008). Astrocytes as determinants
823   of disease progression in inherited amyotrophic lateral sclerosis. Nat Neurosci *11*, 251–
824   253. https://doi.org/10.1038/nn2047.
825   40.   Norden, D.M., and Godbout, J.P. (2013). Review: microglia of the aged brain: primed to
826   be activated and resistant to regulation. Neuropathol Appl Neurobiol *39*, 19–34.
827   https://doi.org/10.1111/j.1365-2990.2012.01306.x.
828   41.   Kobayashi, K., Imagama, S., Ohgomori, T., Hirano, K., Uchimura, K., Sakamoto, K.,
829   Hirakawa, A., Takeuchi, H., Suzumura, A., Ishiguro, N., et al. (2013). Minocycline
830   selectively inhibits M1 polarization of microglia. Cell Death Dis *4*, e525.
831   https://doi.org/10.1038/cddis.2013.54.

42. Zhu, S., Stavrovskaya, I.G., Drozda, M., Kim, B.Y.S., Ona, V., Li, M., Sarang, S., Liu, A.S., Hartley, D.M., Wu, D.C., et al. (2002). Minocycline inhibits cytochrome c release and delays progression of amyotrophic lateral sclerosis in mice. Nature *417*, 74–78. https://doi.org/10.1038/417074a.

43. Tao, J., Wang, H., Wang, W., Mi, N., Zhang, W., Wen, Q., Ouyang, J., Liang, X., Chen, M., Guo, W., et al. (2022). Binding mechanism of oseltamivir and influenza neuraminidase suggests perspectives for the design of new anti-influenza drugs. PLoS Comput Biol *18*, e1010343. https://doi.org/10.1371/journal.pcbi.1010343.

44. Petrov, D., Mansfield, C., Moussy, A., and Hermine, O. (2017). ALS Clinical Trials Review: 20 Years of Failure. Are We Any Closer to Registering a New Treatment? Front Aging Neurosci *9*, 68. https://doi.org/10.3389/fnagi.2017.00068.

45. Katyal, N., and Govindarajan, R. (2017). Shortcomings in the Current Amyotrophic Lateral Sclerosis Trials and Potential Solutions for Improvement. Front Neurol *8*, 521. https://doi.org/10.3389/fneur.2017.00521.

46. Tzeplaeff, L., Jürs, A. V, Wohnrade, C., and Demleitner, A.F. (2024). Unraveling the Heterogeneity of ALS-A Call to Redefine Patient Stratification for Better Outcomes in Clinical Trials. Cells *13*. https://doi.org/10.3390/cells13050452.

47. Achi, E.Y., and Rudnicki, S.A. (2012). ALS and Frontotemporal Dysfunction: A Review. Neurol Res Int *2012*, 806306. https://doi.org/10.1155/2012/806306.

48. Vinsant, S., Mansfield, C., Jimenez-Moreno, R., Del Gaizo Moore, V., Yoshikawa, M., Hampton, T.G., Prevette, D., Caress, J., Oppenheim, R.W., and Milligan, C. (2013). Characterization of early pathogenesis in the SOD1(G93A) mouse model of ALS: part II, results and discussion. Brain Behav *3*, 431–457. https://doi.org/10.1002/brb3.142.

49. Amruta, N., Ismael, S., Leist, S.R., Gressett, T.E., Srivastava, A., Dinnon, K.H., Engler-Chiurazzi, E.B., Maness, N.J., Qin, X., Kolls, J.K., et al. (2022). Mouse Adapted SARS-CoV-2 (MA10) Viral Infection Induces Neuroinflammation in Standard Laboratory Mice. Viruses *15*. https://doi.org/10.3390/v15010114.

50. Bohmwald, K., Gálvez, N.M.S., Ríos, M., and Kalergis, A.M. (2018). Neurologic Alterations Due to Respiratory Virus Infections. Front Cell Neurosci *12*, 386. https://doi.org/10.3389/fncel.2018.00386.

51. Miller, M.S., Rialdi, A., Ho, J.S.Y., Tilove, M., Martinez-Gil, L., Moshkina, N.P., Peralta, Z., Noel, J., Melegari, C., Maestre, A.M., et al. (2015). Senataxin suppresses the antiviral transcriptional response and controls viral biogenesis. Nat Immunol *16*, 485–494. https://doi.org/10.1038/ni.3132.

52. Béland, L.-C., Markovinovic, A., Jakovac, H., De Marchi, F., Bilic, E., Mazzini, L., Kriz, J., and Munitic, I. (2020). Immunity in amyotrophic lateral sclerosis: blurred lines between excessive inflammation and inefficient immune responses. Brain Commun *2*, fcaa124. https://doi.org/10.1093/braincomms/fcaa124.

53. Gerbino, V., Kaunga, E., Ye, J., Canzio, D., O'Keeffe, S., Rudnick, N.D., Guarnieri, P., Lutz, C.M., and Maniatis, T. (2020). The Loss of TBK1 Kinase Activity in Motor Neurons or in All Cell Types Differentially Impacts ALS Disease Progression in SOD1 Mice. Neuron *106*, 789-805.e5. https://doi.org/10.1016/j.neuron.2020.03.005.

54. Dupuis, L., Pradat, P.-F., Ludolph, A.C., and Loeffler, J.-P. (2011). Energy metabolism in amyotrophic lateral sclerosis. Lancet Neurol *10*, 75–82. https://doi.org/10.1016/S1474-4422(10)70224-6.

55. Martin, L.J. (2010). Mitochondrial and Cell Death Mechanisms in Neurodegenerative Diseases. Pharmaceuticals (Basel) *3*, 839–915. https://doi.org/10.3390/ph3040839.

56. Fernández-Beltrán, L.C., Godoy-Corchuelo, J.M., Losa-Fontangordo, M., Williams, D., Matias-Guiu, J., and Corrochano, S. (2021). A Transcriptomic Meta-Analysis Shows Lipid Metabolism Dysregulation as an Early Pathological Mechanism in the Spinal Cord of SOD1 Mice. Int J Mol Sci *22*. https://doi.org/10.3390/ijms22179553.

57. Radigan, K.A., Nicholson, T.T., Welch, L.C., Chi, M., Amarelle, L., Angulo, M., Shigemura, M., Shigemura, A., Runyan, C.E., Morales-Nebreda, L., et al. (2019). Influenza A Virus Infection Induces Muscle Wasting via IL-6 Regulation of the E3 Ubiquitin Ligase Atrogin-1. J Immunol *202*, 484–493. https://doi.org/10.4049/jimmunol.1701433.

58. Kriz, J., Nguyen, M.D., and Julien, J.-P. (2002). Minocycline slows disease progression in a mouse model of amyotrophic lateral sclerosis. Neurobiol Dis *10*, 268–278. https://doi.org/10.1006/nbdi.2002.0487.

59. Drachman, D.B., Frank, K., Dykes-Hoberg, M., Teismann, P., Almer, G., Przedborski, S., and Rothstein, J.D. (2002). Cyclooxygenase 2 inhibition protects motor neurons and prolongs survival in a transgenic mouse model of ALS. Ann Neurol *52*, 771–778. https://doi.org/10.1002/ana.10374.

60. Kiaei, M., Petri, S., Kipiani, K., Gardian, G., Choi, D.-K., Chen, J., Calingasan, N.Y., Schafer, P., Muller, G.W., Stewart, C., et al. (2006). Thalidomide and lenalidomide extend survival in a transgenic mouse model of amyotrophic lateral sclerosis. J Neurosci *26*, 2467–2473. https://doi.org/10.1523/JNEUROSCI.5253-05.2006.

61. Stacey, H.D., Golubeva, D., Posca, A., Ang, J.C., Novakowski, K.E., Zahoor, M.A., Kaushic, C., Cairns, E., Bowdish, D.M.E., Mullarkey, C.E., et al. (2021). IgA potentiates NETosis in response to viral infection. Proc Natl Acad Sci U S A *118*. https://doi.org/10.1073/pnas.2101497118.

62. Leist, S.R., Dinnon, K.H., Schäfer, A., Tse, L. V, Okuda, K., Hou, Y.J., West, A., Edwards, C.E., Sanders, W., Fritch, E.J., et al. (2020). A Mouse-Adapted SARS-CoV-2 Induces Acute Lung Injury and Mortality in Standard Laboratory Mice. Cell *183*, 1070–1085.e12. https://doi.org/10.1016/j.cell.2020.09.050.

63. Durkin, M.E., Qian, X., Popescu, N.C., and Lowy, D.R. (2013). Isolation of Mouse Embryo Fibroblasts. Bio Protoc *3*. https://doi.org/10.21769/bioprotoc.908.

64. Richner, M., Jager, S.B., Siupka, P., and Vaegter, C.B. (2017). Hydraulic Extrusion of the Spinal Cord and Isolation of Dorsal Root Ganglia in Rodents. J Vis Exp *2017*, 55226. https://doi.org/10.3791/55226.

65. Dobin, A., Davis, C.A., Schlesinger, F., Drenkow, J., Zaleski, C., Jha, S., Batut, P., Chaisson, M., and Gingeras, T.R. (2013). STAR: ultrafast universal RNA-seq aligner. Bioinformatics *29*, 15–21. https://doi.org/10.1093/bioinformatics/bts635.

66. Anders, S., Pyl, P.T., and Huber, W. (2015). HTSeq--a Python framework to work with high-throughput sequencing data. Bioinformatics *31*, 166–169. https://doi.org/10.1093/bioinformatics/btu638.

67. Robinson, M.D., McCarthy, D.J., and Smyth, G.K. (2010). edgeR: a Bioconductor package for differential expression analysis of digital gene expression data. Bioinformatics *26*, 139–140. https://doi.org/10.1093/bioinformatics/btp616.

68. Robinson, M.D., and Oshlack, A. (2010). A scaling normalization method for differential expression analysis of RNA-seq data. Genome Biol *11*, R25. https://doi.org/10.1186/gb-2010-11-3-r25.

69. Law, C.W., Chen, Y., Shi, W., and Smyth, G.K. (2014). voom: Precision weights unlock linear model analysis tools for RNA-seq read counts. Genome Biol *15*, R29. https://doi.org/10.1186/gb-2014-15-2-r29.

70. Ritchie, M.E., Phipson, B., Wu, D., Hu, Y., Law, C.W., Shi, W., and Smyth, G.K. (2015). limma powers differential expression analyses for RNA-sequencing and microarray studies. Nucleic Acids Res *43*, e47. https://doi.org/10.1093/nar/gkv007.

71. Mootha, V.K., Lindgren, C.M., Eriksson, K.-F., Subramanian, A., Sihag, S., Lehar, J., Puigserver, P., Carlsson, E., Ridderstråle, M., Laurila, E., et al. (2003). PGC-1alpha-responsive genes involved in oxidative phosphorylation are coordinately downregulated in human diabetes. Nat Genet *34*, 267–273. https://doi.org/10.1038/ng1180.

72. Shannon, P., Markiel, A., Ozier, O., Baliga, N.S., Wang, J.T., Ramage, D., Amin, N., Schwikowski, B., and Ideker, T. (2003). Cytoscape: a software environment for integrated models of biomolecular interaction networks. Genome Res *13*, 2498–2504. https://doi.org/10.1101/gr.1239303.

Figure 1: Acute IAV infection prior to ALS onset accelerates disease progression in SOD1^{G93A} mice
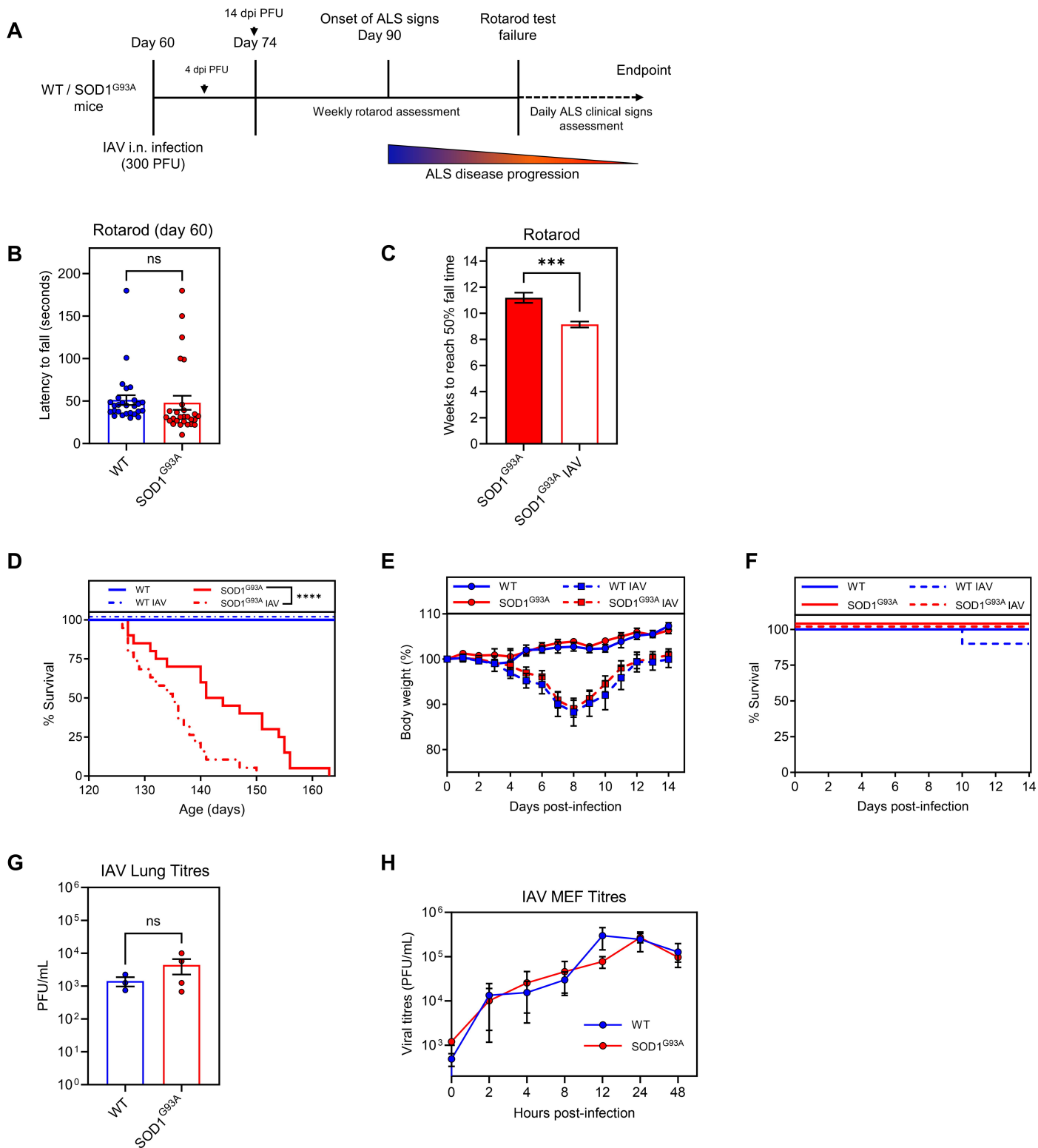

Figure 1. Acute IAV infection prior to ALS onset accelerates disease progression in SOD1^{G93A} mice. A) Schematic of the experimental timeline for IAV infection of mice. **B)** Raw rotarod test fall times of wildtype (WT) (n=9) and SOD1^{G93A} (n=9) mice at day 60 of age. **C)** Weeks for IAV infected (n=14) and control (n=11) SOD1^{G93A} mice to reach 50% of their initial fall time. **D)** ALS-related endpoint (survival) of uninfected WT (n=9) and SOD1^{G93A} (n=20) and IAV infected WT (n=8) and SOD1^{G93A} (n=19) mice. **E)** Weight loss following IAV infection of WT (n=10) and SOD1^{G93A} (n=19) mice as compared to mock-infected WT (n=8) and SOD1^{G93A} (n=10) mice. **F)** Survival of mice following IAV infection. **G)** Lung viral titers 4 days post-IAV infection of WT (n=3) and SOD1^{G93A} (n=4) mice. **H)** Viral growth curves in WT and SOD1^{G93A} mouse embryonic fibroblasts (MEFs) infected with IAV (MOI = 3). Means and standard error of the mean (SEM) are shown. Statistics were obtained by a Student's T-test, one-way ANOVA with Tukey post-hoc test, and Mantel-Cox test. ***, $p < 0.001$. ****, $p < 0.0001$, ns indicates not significant.

# Figure 2: WT and SOD1^(G93A) mice mount similar antiviral- and pro-inflammatory responses following IAV infection
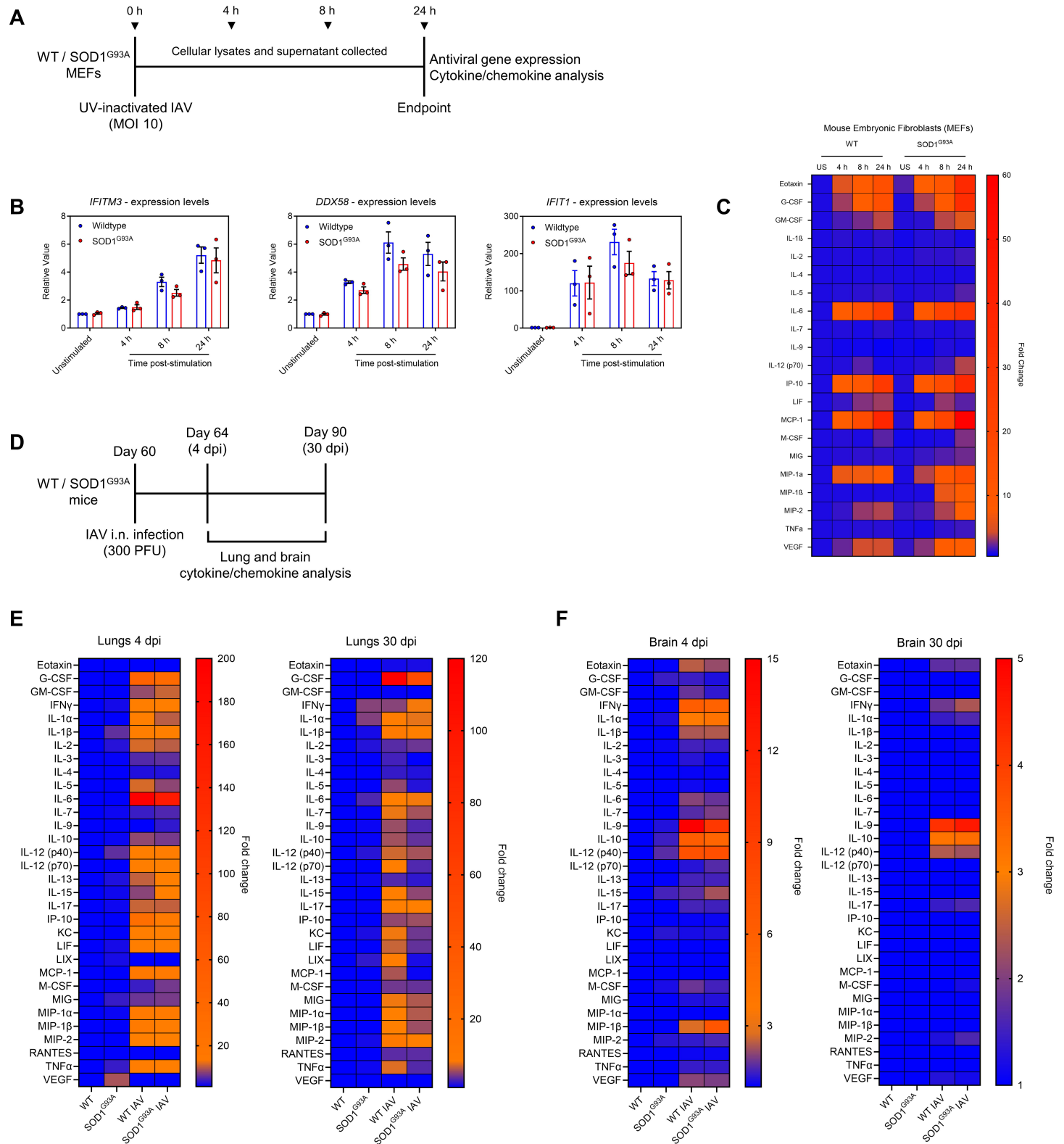
Figure 2. WT and SOD1^(G93A) mice mount similar antiviral- and pro-inflammatory responses following IAV infection. A) Schematic of experimental timeline for assessing antiviral gene and cytokine/chemokine expression in MEFs. B) RT-qPCR of antiviral gene transcript levels in MEF cellular lysates following UV-inactivated IAV stimulation (MOI=10), n=3. Values are normalized to unstimulated WT MEFs C) Pro-inflammatory cytokine expression levels in the supernatant of MEFs following stimulation with UV-inactivated IAV (MOI = 10 equivalent) n=5. Values are normalized to unstimulated (US) WT MEFs. D) Experimental timeline for assessing cytokine/chemokine expression in the lungs and brain. Pro-inflammatory cytokine expression levels in E) the lungs (n=3) and F) the brain (n=3) of uninfected WT and SOD1^(G93A) mice and IAV-infected WT and SOD1^(G93A) mice at 4- and 30- dpi. Values are normalized to uninfected WT mice. Means and standard error of the mean (SEM) are shown.

Figure 3: Virus-induced systemic and neuroinflammation is associated with accelerated ALS disease progression
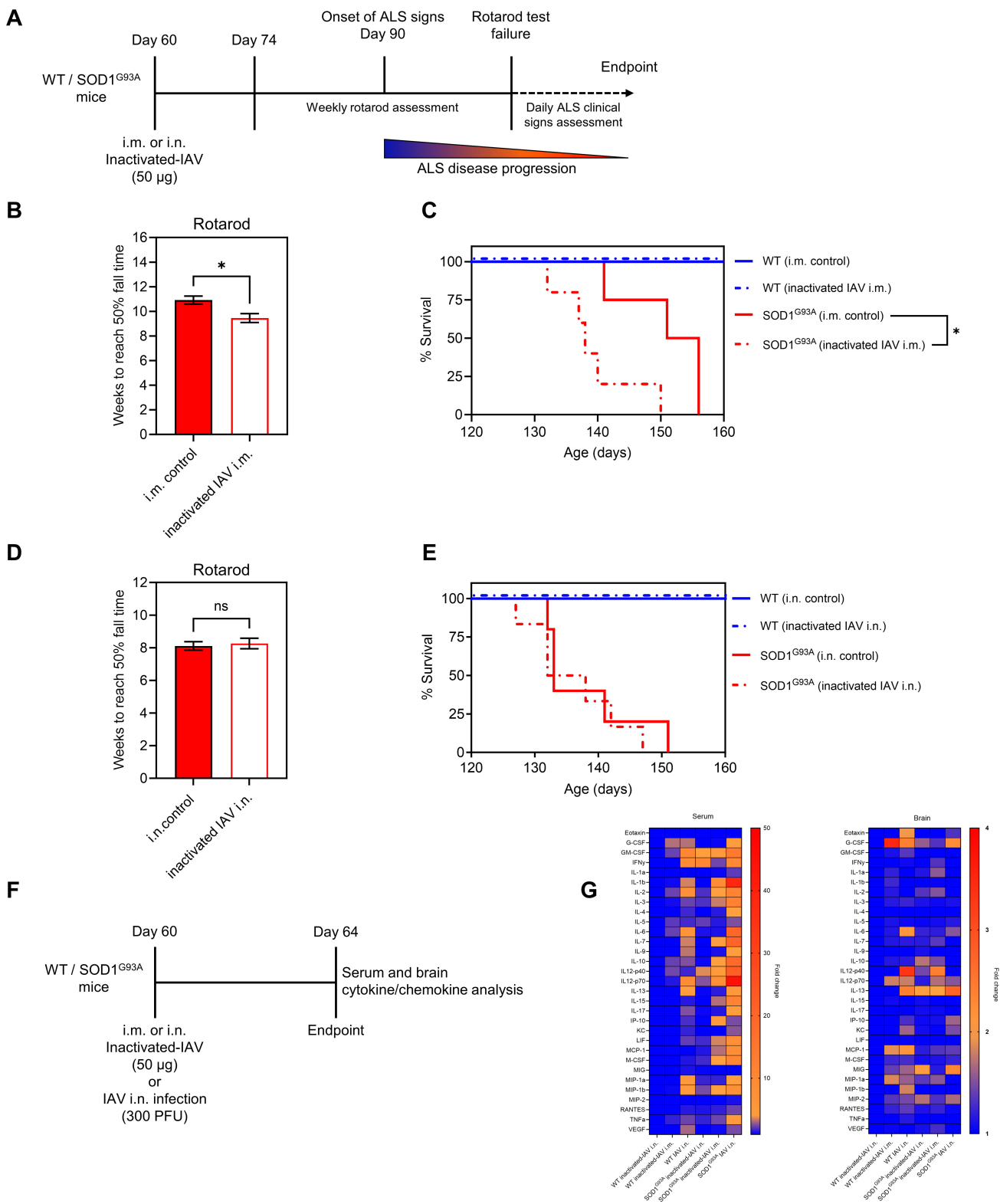

Figure 3. Virus-induced systemic and neuroinflammation is associated with accelerated ALS disease progression. A) Schematic of experimental timeline. **B)** Weeks for mock-injected WT (n=4) and SOD1^{G93A} (n=4) and i.m. inactivated-IAV treated (50 µg) WT (n=11) and SOD1^{G93A} (n=5) mice to reach 50% of their initial fall time. **C)** ALS-related endpoint of WT and SOD1^{G93A} mice administered inactivated-IAV i.m. compared to mice given vehicle control i.m. **D)** Weeks for mock-inoculated WT (n=6) and SOD1^{G93A} (n=5) and i.n. inactivated-IAV treated (50 µg) WT (n=8) and SOD1^{G93A} (n=6) mice to reach 50% of their initial fall time. **E)** ALS-related endpoint of WT and SOD1^{G93A} mice administered inactivated-IAV i.n. compared to mice given vehicle control i.n. **F)** Schematic of experimental timeline to assess cytokine/chemokine production. **G)** Heat-map of cytokine/chemokine expression levels in the serum and brain 4 days post-administration. Means and standard error of the mean (SEM) are shown. Statistics were obtained by a Student's T-test and Mantel-Cox test. *, p < 0.05, ns indicates not significant.

Figure 4: Acute IAV infection is associated with elevated gliosis and ALS-related transcripts in the lumbar spine
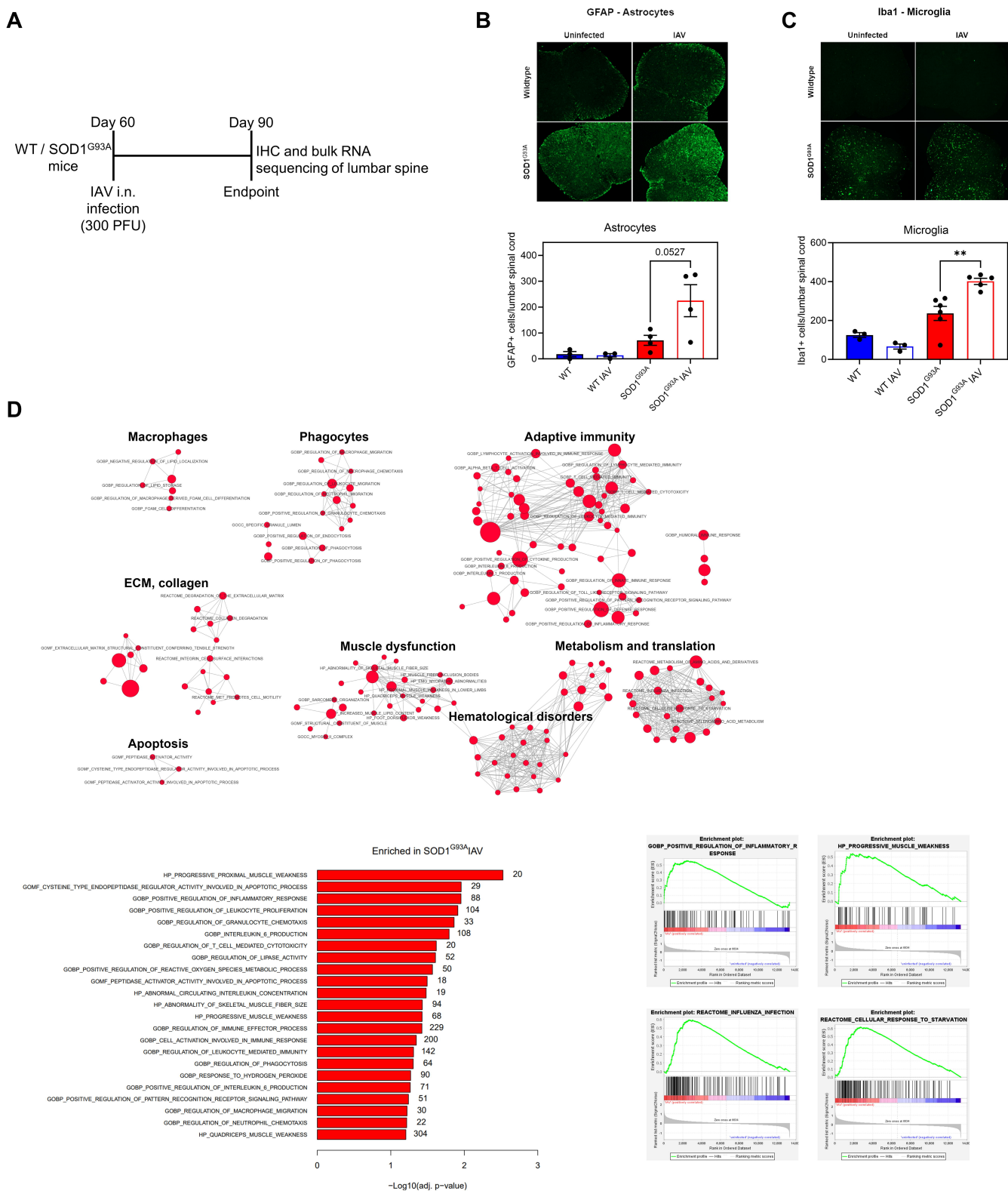

Figure 4. Acute IAV infection is associated with elevated gliosis and ALS-related transcripts in the lumbar spine. A) Schematic for assessing glial cell activation and transcriptomics in the lumbar spine. **B)** Representative images of the lumbar spine sections probed for GFAP (**top**) and quantification of GFAP+ cells for each lumbar spine at day 90 of age (30 dpi) (**bottom**). **C)** Representative images of the lumbar spine sections probed for Iba1 (**top**) and quantification of Iba1+ cells for each lumbar spine at day 90 of age (30 dpi) (**bottom**). Images were taken at 5X magnification. **D)** Gene set enrichment analysis of pathways significantly enriched in IAV infected SOD1^{G93A} mice (n=3) compared to uninfected SOD1^{G93A} mice (n=3) at day 90 of age (30 dpi). Enrichment map (**top**), select enriched pathways with the number of genes associated with each pathway listed beside the bars (**bottom left**), individual enrichment score plots (**bottom right**). Means and standard error of the mean (SEM) are shown. Statistics were obtained by a one-way ANOVA with Tukey post-hoc test. **, p < 0.01.

Figure 5: Inhibition of microglial activation during acute IAV infection protects SOD1^{G93A} mice from accelerated disease progression
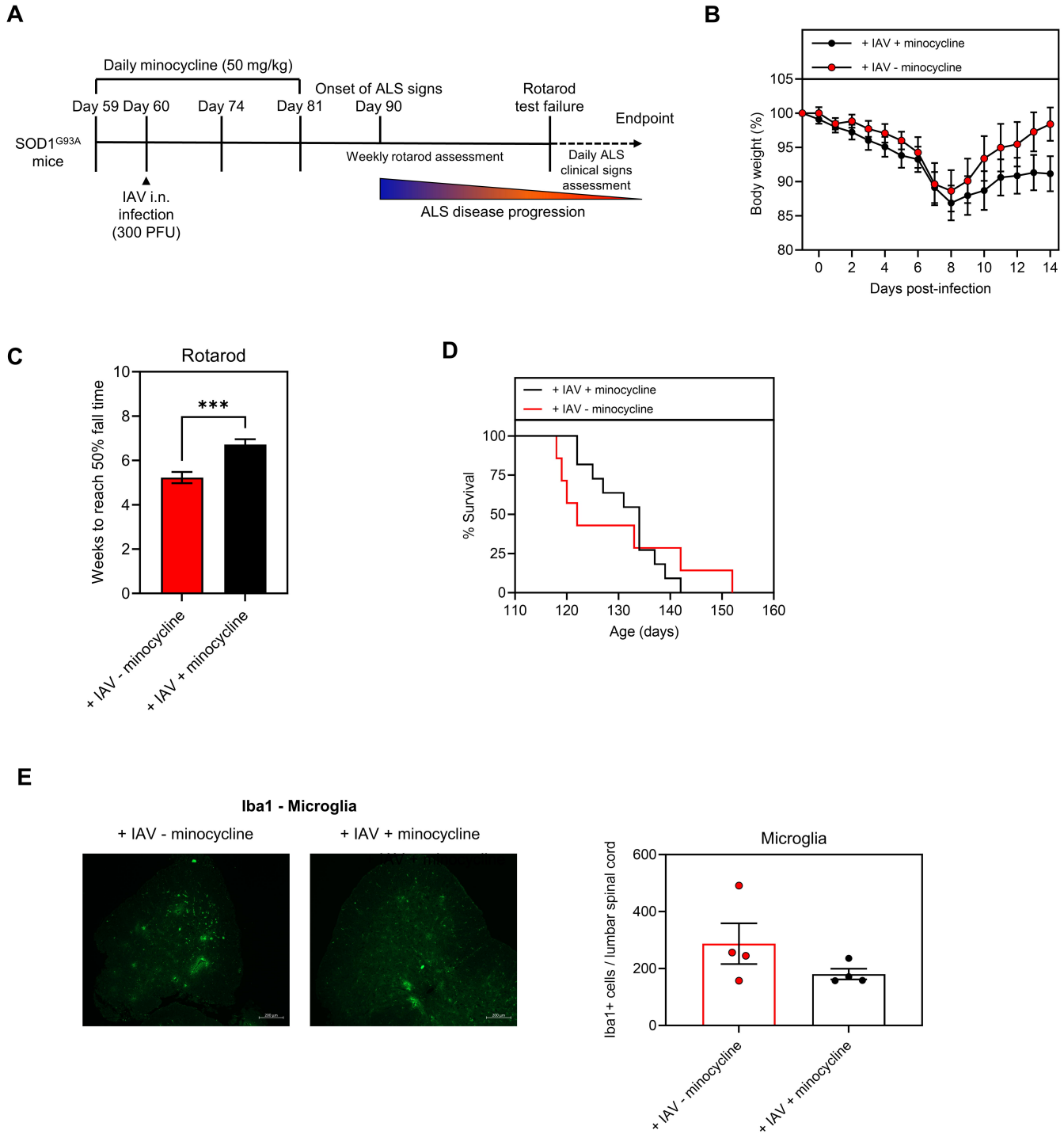

Figure 5. Inhibition of microglial activation during acute IAV infection protects SOD1^{G93A} mice from accelerated disease progression. A) Schematic of experimental timeline. SOD1^{G93A} mice were administered 50 mg/kg minocycline daily at day 59 of age (one day prior to IAV infection) until day 81 of age (3 weeks post-infection). **B)** Weight loss of minocycline treated (n=12) and control (n=8) SOD1^{G93A} mice following IAV infection. **C)** Weeks for minocycline treated and IAV infected (n=11) SOD1^{G93A} mice and IAV infected SOD1^{G93A} mice given vehicle control (n=7) to reach 50% of their initial fall time. **D)** Survival of IAV infected minocycline treated mice compared to IAV infected control. **E)** Representative images (**left**) and Iba1 quantification (**right**) in the lumbar spine at day 81 of age (administration cessation) of IAV infected SOD1^{G93A} mice given minocycline or vehicle control. Images were obtained at 5X magnification. Means and standard error of the mean (SEM) are shown. Statistics were obtained by a Student's T-test, and Mantel-Cox test. ***, p < 0.001.

Figure 6: Oseltamivir treatment during IAV infection protects SOD1^{G93A} mice from accelerated disease progression
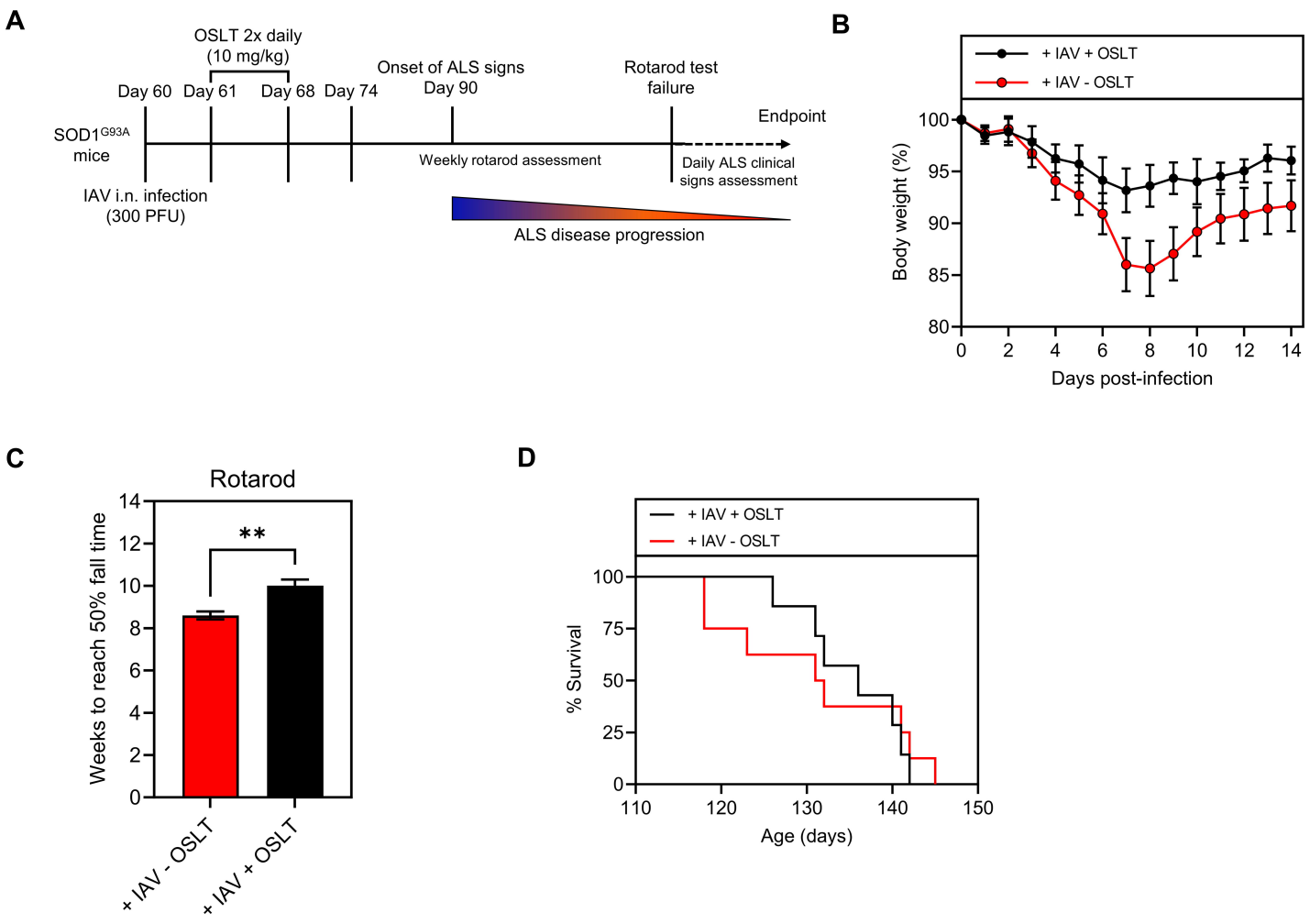
Figure 6. Oseltamivir treatment during IAV infection protects SOD1^{G93A} mice from accelerated disease progression. A) Schematic of experimental timeline. SOD1^{G93A} mice were infected with 300 PFU IAV and treated with oseltamivir (OSLT) via oral gavage twice daily at a dose of 10 mg/kg 1 day following infection. **B)** Weight loss of IAV infected OSLT treated (n=6), IAV infected untreated (n=9) SOD1^{G93A} mice. **C)** Weeks for IAV infected OSLT treated (n=7) and IAV infected vehicle control treated (n=7) mice to reach 50% of their initial fall. **D)** Survival of OSLT treated and untreated, IAV infected SOD1^{G93A} mice due to ALS clinical signs. Means and standard error of the mean (SEM) are shown. Statistics were obtained by Student's T-test, and Mantel-Cox test. **, $p < 0.01$.

Figure 7: SARS-CoV-2 infection prior to ALS onset accelerates disease progression in SOD1^{G93A} mice
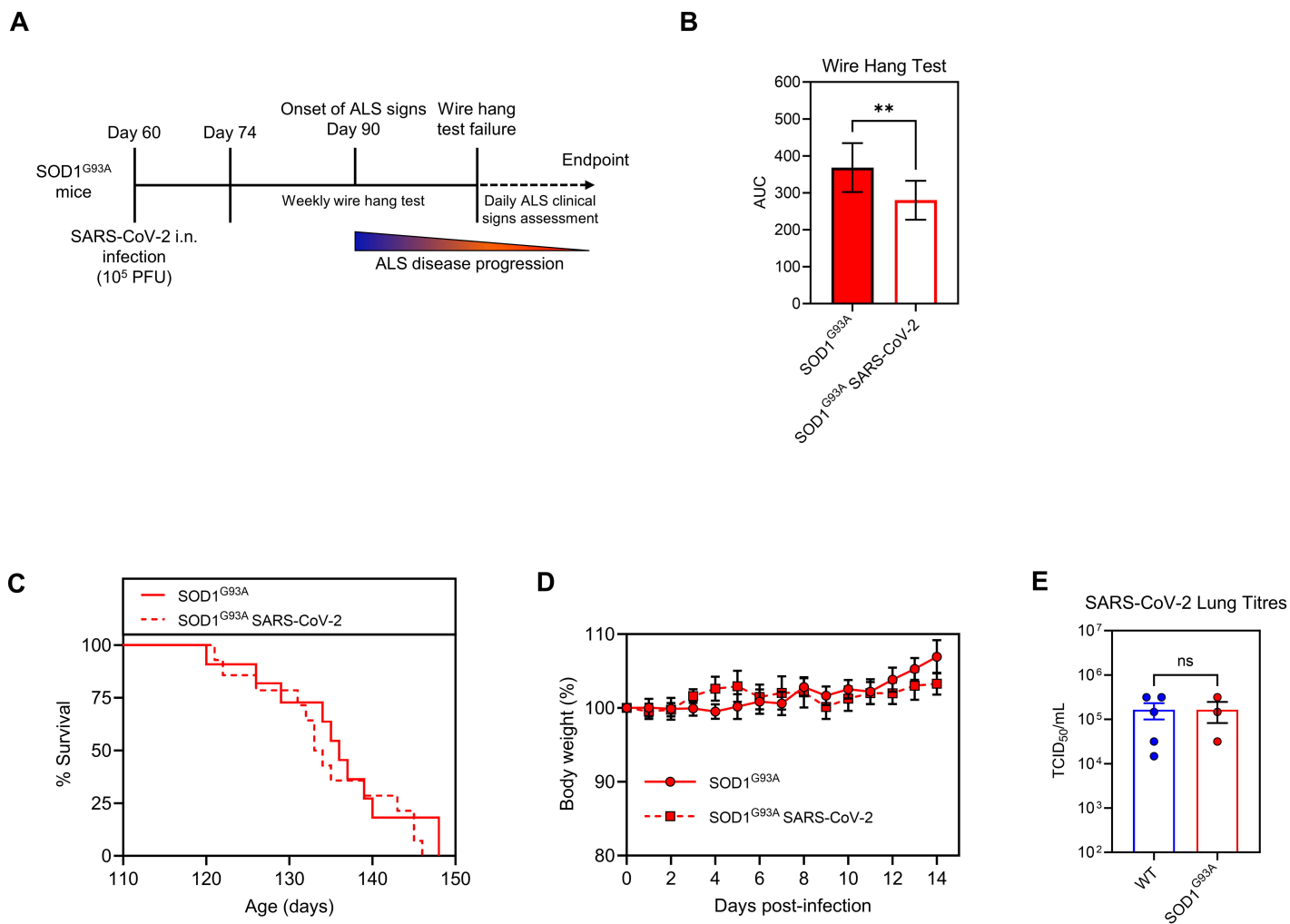
Figure 7. SARS-CoV-2 infection prior to ALS onset accelerates disease progression in SOD1^{G93A} mice. A) Schematic of the experimental timeline for SARS-CoV-2 infection of mice. **B)** Wire hang test evaluation (area under the curve (AUC)) of uninfected SOD1^{G93A} (n = 11) and SARS-CoV-2 infected SOD1^{G93A} (n = 12) mice. **C)** Survival of uninfected SOD1^{G93A} (n = 11) and SARS-CoV-2 infected SOD1^{G93A} (n = 12) mice due to ALS-related endpoint. **D)** Weight loss following SARS-CoV-2 infection, n = 5 - 6. **E)** Viral titres in the lungs at 2 dpi (n = 4). AUC analysis depicts standard deviation. Statistics were obtained by a Student's T-test and Mantel-Cox test. **, $p < 0.01$, ns indicates not significant.